nature reviews methods primers

https://doi.org/10.1038/s43586-024-00366-8

Primer

Check for updates

X-ray absorption spectroscopy

Christopher T. Chantler [1] ✉, Grant Bunker [2] ✉, Paola D'Angelo [3] ✉ & Sofia Diaz-Moreno [4] ✉

Abstract

X-ray absorption spectroscopy (XAS) is an established experimental technique for studying the electronic and local geometric structures of materials. As a short-range order structural probe, it can be applied to all states of matter: crystalline or amorphous solids, liquids and gases. The method is element selective and highly sensitive, with little compromise required to integrate complex sample environment set-ups. These characteristics make the technique suitable for applications in a range of scientific disciplines, from chemistry and catalysis to environmental science, materials science, physics, biology, medicine and cultural heritage. An XAS spectrum is obtained by measuring the modulation of the sample absorption coefficient as a function of the incident X-ray beam energy. Data are usually collected in transmission detection mode, although fluorescence and electron yield detection modes are often used. The XAS spectrum is divided into two regimes: X-ray absorption near-edge structure and extended X-ray absorption fine structure. In this Primer, an overview of XAS fundamentals is given, together with a description of the experimental set-ups, sample requirements, data analysis and possible applications.

Sections

[1]School of Physics, The University of Melbourne, Parkville, Victoria, Australia. [2]Department of Physics, Illinois Institute of Technology, Chicago, IL, USA. [3]Department of Chemistry, University of Roma 'La Sapienza', Rome, Italy. [4]Diamond Light Source, Didcot, UK. ✉e-mail: chantler@unimelb.edu.au; bunker@iit.edu; p.dangelo@uniroma1.it; sofia.diaz-moreno@diamond.ac.uk

Introduction

X-ray absorption spectroscopy (XAS) measures the transmission of a substance as a function of the incident photon energy E in the X-ray regime. It is element-specific and orbital-specific, enabling the local atomic and electronic structure of matter to be determined. It can derive oxidation states, density of states, coordination, bond lengths, thermal parameters and disorder in a local environment, in principle to much higher accuracy than other techniques. As XAS does not depend on long-range order, it is particularly suited to studying disordered systems that have local short-range order, for example, glasses, solutions, liquids and non-crystalline solids. However, it can also be applied to well-defined or even ideal crystals. XAS can confirm structures suggested by other techniques, or disprove a hypothesis in favour of a valid local structure, based on nanostructure, local bonding and nano-environment around the absorbing atomic species. Although XAS can be performed with laboratory X-ray sources, it is more commonly performed at a synchrotron. Most synchrotrons have dedicated beamlines for XAS, which is one of the three most common synchrotron techniques, alongside powder diffraction and single-crystal diffraction. It is complementary to many other techniques and can provide unique insights.

Conventionally, XAS includes X-ray absorption fine structure (XAFS) and the overall XAS spectrum can be divided into two regions (Fig. 1d): the X-ray absorption near-edge structure (XANES) and extended XAFS (EXAFS). XANES is often investigated by fingerprinting or linear component fitting and involves complex excitation theory using molecular orbital principles or multiple-path, multiple-leg scattering — two-leg or three-leg paths with multiple scattering — of the photoelectron. The EXAFS region is fit with a range of available theories and software packages. The complex oscillatory structure observed in XAS arises from quantum interference between the photoelectron wave emitted above a photoabsorption edge (Fig. 1a) and elastically scattered photoelectron waves from neighbouring charge density (Fig. 1c). This can determine the oxidation state, geometry and structure of the local environment around the absorbing atom[1]. In addition, the XANES region includes pre-edge features, which correspond to bound–bound resonant excitations that can explain the geometry, coordination and oxidation state of the absorbing atom[2].

Early studies of X-ray spectroscopy (Box 1) used laboratory sources with low energy resolution and large beam divergence. When synchrotrons and synchrotron beamlines were developed, the flux and statistics of the X-ray spectra, XAS and XAFS, improved markedly. This includes higher energy resolution from higher-order monochromator crystal diffraction planes. Recently, laboratory sources have been revisited and optimized and are now much more useful to characterize a range of ideal or traditional samples using transmission detection mode and fluorescence detection mode. X-ray free electron lasers (XFELs) have even higher brilliance than synchrotrons, with experimental optics that need to handle increased flux on a smaller target cross-section.

An XAS spectrum may also be obtained using fluorescence detection (Fig. 1b), electron yield and scattering processes indirectly without direct measurement of X-ray absorption. Some experimental set-ups use partial fluorescence yield or fluorescence detection with a region of interest selected to correspond to a particular emission line[1]. The nomenclature used throughout this Primer follows the definitions in refs. 2–4.

X-ray absorption coefficient and cross-sections

Figure 2a shows a log–log plot of the photoelectric X-ray mass absorption coefficient $[\mu/\rho]_{pe}(E)$, which is proportional to the cross-section for absorption σ_{pe} versus X-ray photon energy E for the pure element platinum. The total (inelastic + elastic) scattering cross-section and total mass attenuation coefficient $[\mu/\rho]_{pe}(E)$ are also shown. The source data for the plot are the FFAST database at NIST[5,6], which provides spectra computed relativistically for an atomic system, meaning that it does not include the XAFS fine structure. The general trends are of key importance when planning XAFS experiments[7–9].

If more than one element is present in the sample, for the purpose of planning an experiment, the total photoelectric mass absorption coefficient $[\mu/\rho]_{pe}(E)$ may be approximated as:

$$\left[\frac{\mu}{\rho}\right]_{pe}(E)\rho = \sum_i \rho_i \left[\frac{\mu}{\rho}\right]_{pe,i}(E) = \rho \sum_i f_i \left[\frac{\mu}{\rho}\right]_{pe,i}(E), \quad (1)$$

in which $[\mu/\rho]_{pe,i}(E)$ and ρ_i are, respectively, the photoelectric mass absorption coefficient and the mass density of the ith material in the sample; or alternatively expressed, ρ is the total mass density of the sample and f_i is the mass fraction of the ith element in the sample. This expression is approximate because it does not describe changes in absorption owing to interactions between atoms, which are of key interest in XAFS. Additionally, the sum is correct for photoelectric absorption, but only approximate for coherent or incoherent scattering contributions.

Figure 2a,b shows log–log plots showing the dramatic changes that occur in absorption as a function of energy. As X-ray energy increases, the X-ray becomes more penetrating — the absorption cross-section decreases — except at certain specific energies that are characteristic of the atomic element, in which absorption suddenly increases. These absorption edges occur at energies where the photon has sufficient energy to excite an electron bound in an inner atomic orbital to an unfilled state of appropriate symmetry in the continuum. The K-edge is the highest energy edge, with an electron being ejected from the $n=1$, K atomic shell or the 1s state. The L-edges originate from the $n=2$, L shell, including the 2s state, referred to as the L_1-edge, which is the highest energy L-edge; the $2p_{1/2}$ state, which corresponds to the L_2-edge; and the $2p_{3/2}$ representing the L_3-edge, the lowest energy L-edge (Fig. 1a). Generally, each edge will probe final states of different symmetries, which can be useful experimentally. Often, the practical choice of which edge to probe is based on energy accessibility at the available beamlines.

Between the absorption edges in the log–log plot of Fig. 2, the cross-section and mass absorption coefficient are close to a straight line, which indicates power-law behaviour. To a useful approximation, the cross-section of all materials decreases approximately as $1/E^3$ between absorption edges, so halving the energy increases the absorption coefficient by about a factor of eight, as long as there are no edges between the two energies. As the transmitted flux varies as $\exp(-\mu(E)t)$, this strong energy dependence can have a dramatic effect on the penetration depth of X-rays, which is important to consider when designing experiments and instrumentation for lower X-ray energies. As a result, it is essential to calculate or look up absorption values during experiment design.

The desired element can be selected by measuring $\mu(E)$ over one of its edges. The K-edge energies vary approximately with atomic number Z as $E_K \approx Z^{2.16}$, in which the exponent is generally in the range 2.14–2.20 depending on the range of Z that is considered; a hydrogenic atom has exponent of exactly 2. This approximation is useful for a rough estimation of K-edge energies.

The energy dependencies of L-edges and L-edge hole widths are more complex. However, all can be found in advanced references[7,10,11]

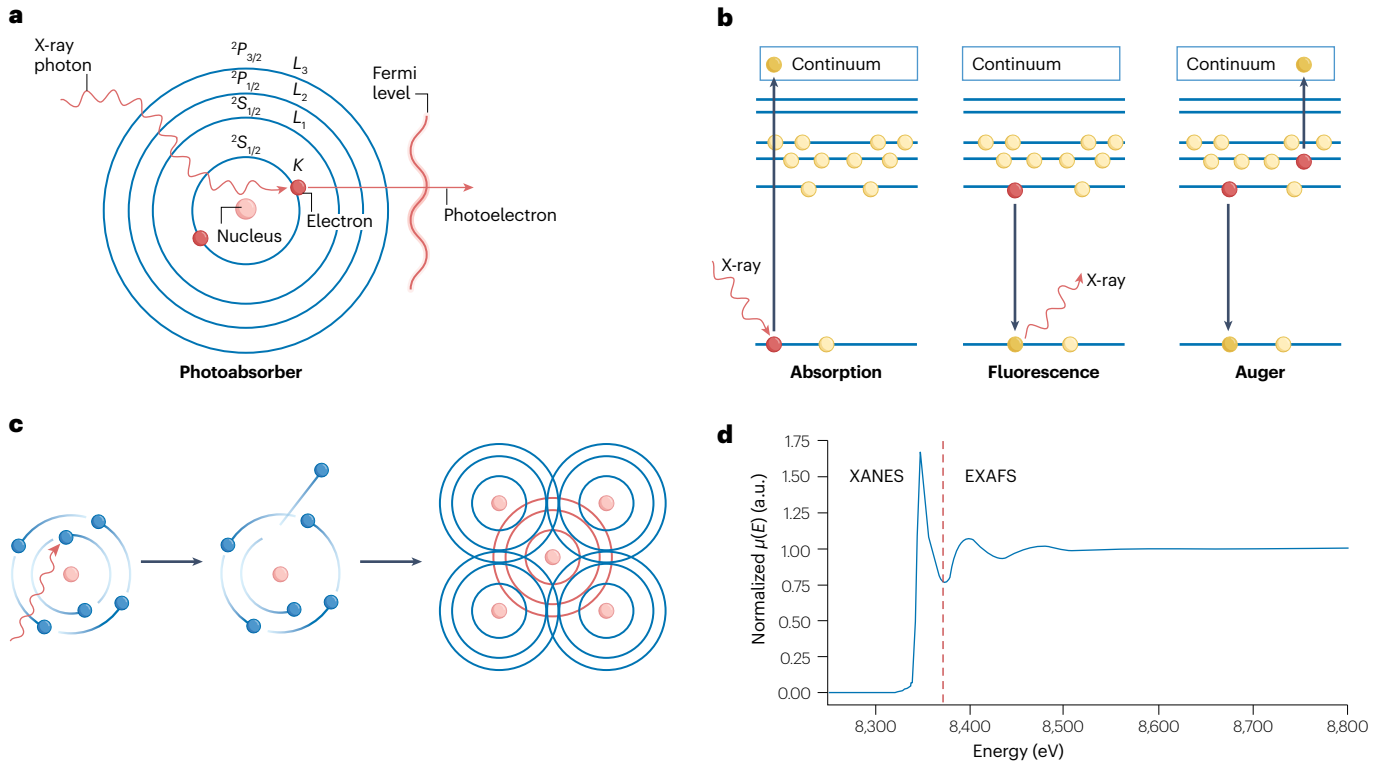

Fig. 1 | Processes in X-ray absorption spectroscopy. a, Representation of the interaction of X-ray photons with an absorbing atom and nomenclature of the absorption edges relative to the inner shell electron states. **b**, Energy level diagrams for the processes of photoabsorption, X-ray fluorescence and Auger photoelectron production. **c**, Schematic picture of the incoming and backscattered photoelectron wave, which illustrates the concept of interference in extended X-ray absorption fine structure (EXAFS). The incident X-ray photon interacts with the absorbing atom. A photoelectron is emitted and backscattered from the surrounding atoms. The backscattered wave from the surrounding atoms interacts with the outgoing wave in a constructive or destructive manner, depending on the energy of the incident X-ray photon. This gives rise to an oscillation in the absorption coefficient that produces an X-ray absorption spectrum. **d**, Typical X-ray absorption spectroscopy spectrum in which the X-ray absorption near-edge structure (XANES) and EXAFS regions are highlighted. a.u., arbitrary units.

or in a simple form at the X-ray data booklet. Care should be taken when calibrating spectra to energies to ensure that the definition of the edge energy matches the experimental method and resolution for measurement[2]. The X-ray attenuation database at NIST[5,6] contains reference values. Other media are also readily available, for example, databases contained within the software packages Hephaestus, Xraylarch, Mathematica (as StoppingPowerData) and others. The online server, Mucal Periodic Table, is useful for quick lookups.

Background theory

When a photon is absorbed by a material following the photoelectric effect, a free photoelectron is emitted into the continuum or bound state. The process is dominated by photon interaction with electrons in the material (Figs. 1 and 2). At high energies, the photon interacts with charge on protons in the nucleus, meaning that nuclear processes and nuclear resonances become dominant. Magnetic interactions also occur and relativistic spin–orbit coupling is crucial, but magnetic coupling is normally small compared with photoabsorption and electron emission. The starting point for understanding XAS is perturbation theory for the photoabsorption cross-section, amplitude, matrix element or form factor and equations for the perturbing time-dependent Hamiltonian[1]. The transition rate and whole XAFS interference signal arise, in second-order perturbation theory, from the second term of the Born sequence: interference of the returning electron wave. This interference may be compared with the first-order cross-section – the atomic or reference absorption coefficient – without potential scattering of the photoelectron wave. Transition matrix or Green's function approaches[12–15] require higher-order perturbation theory.

Elastic scattering – which yields a secondary photon with the same energy and wavelength, scattered through some angle – is the basis of X-ray diffraction and thermal diffuse scattering and is stronger at higher energies. Elastic interactions[16–18] include scattering from bound electrons, referred to as Rayleigh scattering[19,20], with transition amplitude A^R and cross-section in barns per atom σ_R; scattering from the proton charge in the nucleus, known as nuclear Thomson scattering[21], with amplitude A^{NT} and cross-section σ_{NT}; Delbruck scattering[22,23] (A^D, σ_D) from virtual electron–positron pairs created in the screened nuclear Coulomb potential occurs due to vacuum polarization and quantum electrodynamics in the photon energy range 100–1,000 keV; and nuclear resonance scattering[24] (A^{NR}, σ_{NR}) from nuclear collective resonances at much higher energies. Elastic processes yield a photon with the same energy as the incident photon, making them coherent and the amplitudes add in phase:

$$A^{\text{elastic}} = A^R + A^{NT} + A^D + A^{NR}, \quad (2)$$

Box 1 | Key historical advances

- 1913: the first measurements of X-ray absorption edges, understanding of absorption edges and the Periodic Table[272].
- 1913: the first X-ray absorption edges in silver and bromine[273].
- 1914: proposal that each absorption edge corresponds to excitation of an electron from a particular bound orbital into the continuum[273].
- 1920: recording of the first X-ray absorption spectroscopy spectrum that shows modulation of the absorption coefficient[274].
- 1932: short-range order theory developed for molecules and proposal that structure comes from interference by near-neighbour atoms only.
- 1970: point-scattering model developed to predict structure based on a sum of wavefunctions reflected from atomic centres in a small cluster. Structure is renamed X-ray absorption fine structure.
- 1971–1975: Fourier transform approach to extended X-ray absorption fine structure made the theory and analysis much more powerful[49–51,275,276].
- 1975–1986: recognition that the photoelectron and returning interferences are spherical wavelets, enabling much greater insight and predictability[27,122,277,278].
- 1977–1978: inclusion of the many-body reduction factor S_0^2 followed[130,279].
- 1981: second-generation, purpose-built synchrotrons introduced, beginning with Daresbury synchrotron.
- 1985: the rigorous link of X-ray wavelengths to visible wavelengths and SI units, such as the metre, was established[7,280,281].
- 1986–2001: developments of the muffin-tin potential approximation; clarification of the Green function approach; higher order and multiple-leg path terms; and cumulant approaches to atomic distribution functions[29,106,282,283].
- 1994: third-generation, modern synchrotron facilities with specialized insertion devices (wiggler magnets and undulators) introduced to increase irradiance and modify beam characteristics, beginning with the European synchrotron radiation facility.
- 1998 onwards: recent techniques[98,115,180,255,256,284–286].

The elastic or coherent cross-section $\sigma_{elastic} = \sigma_{coh}$ is proportional to $[A^{elastic}]^2$. Inelastic scattering of the photon yields an excited state and a photon is emitted at a lower energy. Inelastic scattering processes are dominant at higher energies and include photoexcitation, such as photoabsorption from photoionization; Compton scattering from a free or bound electron[25,26] (A^C, σ_C); electron–positron pair production from the vacuum field of the nucleus (A^n, σ_n), with a threshold above $2m_ec^2$ or 1.022 MeV; triplet production or pair production with electronic excitations (A^e, σ_e) with a similar threshold; photonuclear absorption (A^{pn}, σ_{pn}) yielding the emission of a neutron $\sigma(\gamma, n)$, proton $\sigma(\gamma, p)$ or another particle at much higher energies. Assuming that each process and cross-section is incoherent with other process gives the common formula:

$$\sigma_{tot} = \sigma_{pe} + \sigma_{elastic} + \sigma_C + \sigma_n + \sigma_e + \sigma_{pn}. \quad (3)$$

Following refs. 27,28, the primary functional fitted in XANES should be $\mu_{pe}(E)$ or $[\mu/\rho]_{pe}(E)$ to match the theoretical prediction. By contrast, in conventional XAFS or EXAFS fitting, the relevant functional fitted is:

$$\chi(k) = \frac{\left[\frac{\mu}{\rho}\right]_{tot}(E) - \left[\frac{\mu}{\rho}\right]_0(E)}{\left[\frac{\mu}{\rho}\right]_0(E)}, \quad (4)$$

in which the effective photoelectron wavenumber $k = \sqrt{\frac{2m(E-E_0)}{\hbar^2}} \sim 0.51235\sqrt{E-E_0}$ with E and E_0 in electronvolt and k in per Angstrom (Fig. 1). $[\mu/\rho]_0(E)$ is either the photoabsorption coefficient for an isolated atom with no electron interference, a semi-empirical spline or background-subtraction approximation or an estimated edge-jump amplitude $\Delta\mu_0(E)$ with $\chi(k) = \frac{\mu(E)-\mu_0(E)}{\Delta\mu_0(E)}$. $[\mu/\rho]_{tot}(E)$ is the total measured mass attenuation coefficient; however, it should be replaced by the mass absorption coefficient $[\mu/\rho]_{pe}(E)$. With these various definitions of $\chi(k)$, it is clear that $\chi(k)$ is not a uniquely defined function, and this variation can affect the structure and amplitude of spectra during later analysis. Full-potential codes can fit the XANES, pre-edge and EXAFS regions using $[\mu/\rho]_{pe}(E)$, giving a better match with theoretical computations.

The phenomenological XAFS equation can be used to determine path or bond distances R_j; coordination numbers N_j for equivalent paths in a shell; structural and vibrational variance in paths or bond distances σ_j^2; the many-body amplitude reduction factor for multi-electron processes $S_0^2(k)$; and the effective curved-wave backscattering amplitude, based on:

$$f_{eff}(\theta_i, k, R_j) = |f_{eff}(\theta_i, k, R_j)|e^{i\Phi_{eff,j}} \quad (5)$$

for an $(i+1)$-legged path, with $\theta_{i=1} = \pi$ for a two-legged path. The final-state l-wave central atom phase shift is given by δ_c^l and the mean free path of the photoelectron by $\lambda(k)$ with or without the lifetime hole width of the excited state. For K-edges, L_1-edges and M_1-edges, in which the initial state has $l_0 = 0$, dipole selection rules yield $l = l_0 + 1 = 1$, meaning that the phase offset is dominated by the dipole single-leg offset δ_1; the curved wave offset $\Phi_{eff,j}$ or defect β; and the π phase change. Under these approximations:

$$\chi_{l=0}(k) \sim -\Sigma_j N_j S_0^2(k)\frac{|f_{eff}(\theta_i, k, R_j)|}{kR_j^2}\sin(2kR_j + \delta_j(k)^l + \Phi_{eff,j})e^{-2\sigma_j^2k^2}e^{-2R_j/\lambda(k)}, \delta_j(k) = 2\delta_1 + \beta - \pi \quad (6)$$

Detailed derivations of multiple scattering, convergence of the perturbation series expansion and full potential theory use a more exact quantum mechanical formulation; however, they can be put into the same form as this expression. Cumulant approaches[29,30] replace the Gaussian approximation $e^{-2\sigma_j^2k^2}$ with cumulants of the atomic distribution function. Self-energy, intrinsic losses and more can be seen using $f_{eff}(\theta_i, k, R_j)e^{-2R_j/\lambda(k)}$ terms. For p electron transitions (L II, L III, M II and M III edges) in which the initial state has $l_0 = 1$, and dipole selection rules $l = 0$ or $l = 2$, these approximations give two channels (s and d transitions) which interfere[27,31], corrected from[32]:

$$\chi_{l=1}(k) \sim -\Sigma_j N_j S_0^2(k)\frac{|f_{eff}(\theta_i, k, R_j)|}{kR_j^2} \times ((1-3\cos^2\theta_j)M_{02}\sin(2kR_j + \delta'_{02j}(k)) + \frac{1}{2}(1+3\cos^2\theta_j)\sin(2kR_j + \delta'_{2j}(k)))e^{-2\sigma_j^2k^2}e^{-2R_j/\lambda(k)}, \quad (7)$$

$$M_{02} = (<2|z|1><0|z|1> + <1|z|2><1|z|0>)|<2|z|1>|^{-2}, \delta'_{02j}(k) = \delta_2(k) + \delta_0(k) + \beta_j(k).$$

The components of equation (7) depend on the scattering angle at each reflection, θ_j, which have individual matrix elements M_{02} and phase offsets δ'_{02j} from quadrupole interactions relative to the dipole contributions. Different presentations normalize the matrix elements differently and also include the minor M_{01}^2 term. The extra interference channel is oriented. As a result, it depends on how the incident photon is polarized with the alignment or orientation of any material periodicity. In the absence of alignment, this looks like a different effective scattering factor f_{eff}, but each scattering path or potential has a different phase offset. Therefore, there would be multiple components of interference even for a single two-legged path.

Fluorescence measurement of XAS spectra is common, especially for dilute systems and solutions. In this case, the photoabsorption coefficient is not measured, but rather[33–36]:

$$I_f = \frac{f I_0 \Omega [\mu/\rho]^*_{pe}/(4\pi \cos\theta_{inc})}{[\mu/\rho]/(\cos\theta_{inc}) + [\mu_f/\rho]/(\cos\theta_{out})} \times \left\{1 - \exp\left[-\frac{[\mu/\rho][\rho t]}{\cos\theta_{inc}} - \frac{[\mu_f/\rho][\rho t]}{\cos\theta_{out}}\right]\right\}, \quad (8)$$

in which f is the fluorescence yield given by the region of interest (or the range of emission energies accepted by the detector), for example, K_α fluorescence. The * indicates that only the component that is absorbed by the active atomic orbital producing the fluorescent photon contributes, whereas subscript pe shows that only the photoelectric absorption coefficient is considered, rather than the total attenuation coefficient. Ω is the solid angle subtended by each detector (pixel); θ_{inc} is the incident angle of the X-rays onto the sample relative to the normal; θ_{out} is the angle of emission of the fluorescent radiation from the sample relative to the normal; $[\mu_f/\rho]$ is the mass attenuation coefficient of the material at the energy of the fluorescent photon; t is the sample thickness and I_f is the number of fluorescence photons in a small solid angle Ω centred on θ_{out} (refs. 37–39). As each detector pixel represents a different θ_{out} from the sample surface, there will be a different self-absorption function for each pixel. This is an energy-dependent function.

Defining monitor and detector as the measured counts in the upstream and downstream detectors, respectively; I_f and I_0 as the actual fluxes or counts; ε_{mon} and ε_{det} as the upstream and downstream detector efficiencies; air, w, m and c as the air, window, monitor, gas and other paths, respectively; and A and F as the transmission into (absorption) and out of (fluorescence) the sample gives:

$$\left[\frac{I_f}{I_{0monitor}}\right]_A = \frac{I_f}{I_0}\left[\frac{1}{\varepsilon_{mon}(E)}\right]_A \exp\left[-\left[\frac{([\mu/\rho][\rho t])_{air}}{\cos\theta_{air}}\right]_A - \left[\frac{([\mu/\rho][\rho t])_w}{\cos\theta_w}\right]_A - \left[\frac{([\mu/\rho][\rho t])_m}{\cos\theta_m}\right]_A - \left[\frac{([\mu/\rho][\rho t])_c}{\cos\theta_c}\right]_A\right], \quad (9)$$

$$\left[\frac{I_{fdetector}}{I_{0monitor}}\right]_{measured} = \left[\frac{I_f}{I_{0monitor}}\right]_A [\varepsilon_{det}(E_f)]_F \exp\left[-\left[\frac{([\mu_f/\rho][\rho t])_{air}}{\cos\theta_{air}}\right]_F - \left[\frac{([\mu_f/\rho][\rho t])_w}{\cos\theta_w}\right]_F - \left[\frac{([\mu_f/\rho][\rho t])_m}{\cos\theta_m}\right]_F - \left[\frac{([\mu_f/\rho][\rho t])_c}{\cos\theta_c}\right]_F\right]. \quad (10)$$

Equation (9) can be inverted to correct for absorption and self-absorption in the sample, using packages such as SeAFFluX[35,36]. After inversion, fluorescence does not yield an absolute value of absorption – in the thick sample limit it is independent of thickness – but rather reports $a_i \frac{I_f}{I_0}$ or at best $a_i[\mu/\rho]^*_{pe}(E)[\rho t]$. This can be used effectively, especially if the above-edge distortions are corrected. One of the best approaches is to simultaneously measure in transmission and absorption, which enables the fluorescence signal to be scaled in very close agreement to the theoretical mass absorption coefficient and experimental transmission mass absorption coefficient.

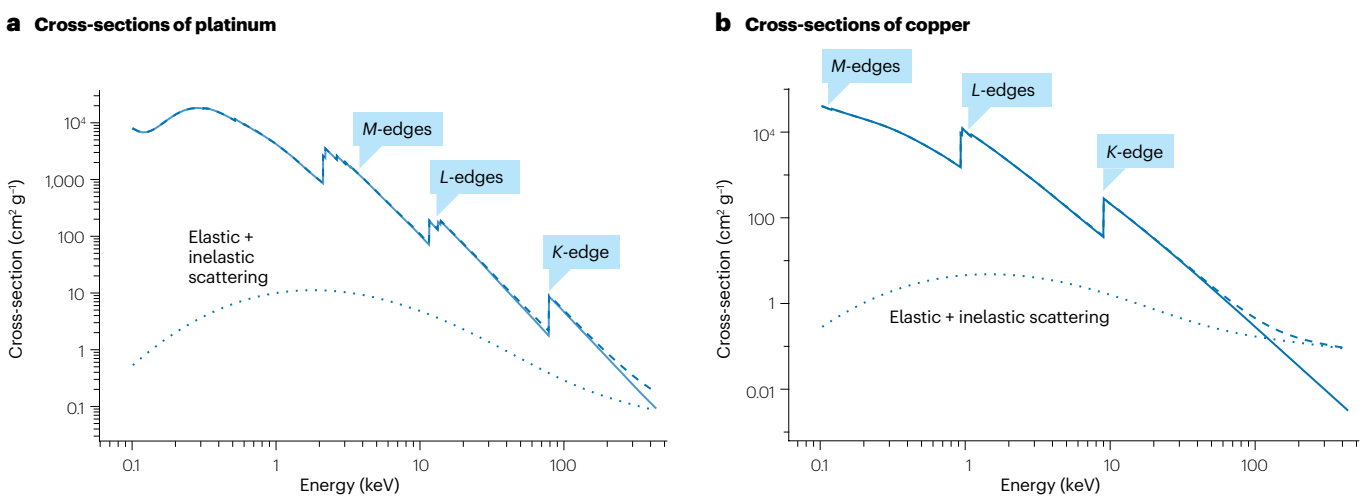

Fig. 2 | Log–log plots of X-ray mass absorption coefficients versus photon energy. a, Plot for the element platinum. **b**, Plot for the element copper. In both panels, the dotted line is scattering and the dashed line is the total (photoelectric absorption with scattering) attenuation coefficient. The relatively straight lines between the absorption edges indicate the approximate power law behaviour of cross-section above and away from edges.

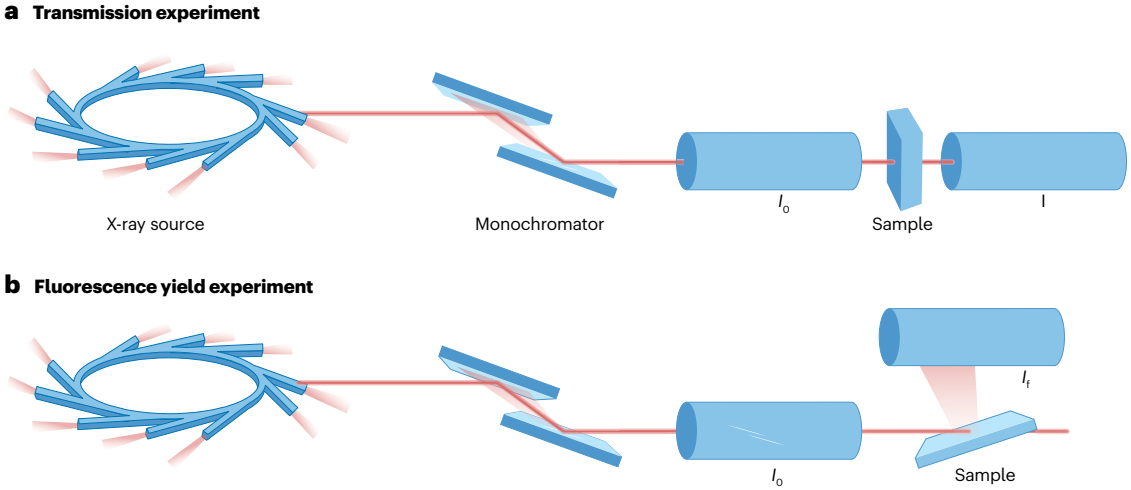

Fig. 3 | Schematic diagram of X-ray absorption fine structure measurements. Transmission experiment set-up (part **a**) and fluorescence yield experiment set-up (part **b**). I_0 is the upstream or monitor flux and I_f is the downstream or detector or fluorescence detector flux. The time for counting is the same. In the first schematic, the flux after attenuation is measured; in the second schematic, the ionized sample emits fluorescence, which is measured.

Primer purpose

The aim of this Primer is to briefly summarize key components of the current XAFS, XANES and EXAFS experimental set-up, theory, analysis and applications, particularly as presented at many international facilities and synchrotrons. It is intended as an introductory guide for users and beamline scientists, without replacing detailed guides, beamline introductions or advanced texts, such as the International Tables for Crystallography[40–43]. This short Primer concentrates on transmission and fluorescence detection mode spectroscopy, XAS and X-ray emission spectroscopy (XES). In some cases, high-energy resolution fluorescence detection (HERFD) is used, in which the bandwidth of the beam or region of interest in fluorescence may be very narrow or mapped across incident energy and emission energy axes in a full 2D spectrum. An example of this is in resonant inelastic X-ray scattering (RIXS), which focuses on the bound–bound resonance processes below the absorption edge and above the Fermi level.

HERFD, RIXS[44,45], total fluorescence yield or secondary process measurement such as total electron yield spectroscopy[46], Auger electron spectroscopy, or other surface spectroscopies, such as RefleXafs[47,48], are not discussed, despite exciting science, potential and applications. Although recent advances of inverse Compton, XFEL and laboratory source applications are not described in this article, most of the discussion is also relevant for those sources and techniques.

Experimentation

XAFS spectroscopy[49–51] studies changes in the X-ray absorption coefficient that occur as a consequence of chemical bonding. Different atomic elements can be targeted by selecting absorption edge energies characteristic of those atoms. A particular strength of XAFS is that it does not require long-range order in the sample, in contrast to classical diffraction methods, so it is applicable to crystals, amorphous systems, polycrystalline solids, alloys, solutions and molecular gases. XAFS also does not have stringent sample or environment requirements, making it feasible for investigating non-ideal, real-world systems. Standard XAFS experimental methods are reviewed in refs. 31,40,41,52,53.

Reliable measurements of XAFS must take into account the general behaviour of X-rays and their interactions with matter — the energy dependence of absorption and scattering — and the specific characteristics of the XAFS measurement process, for example, the energy range, sampling and resolution needed to record a spectrum. Transmission, the simplest and most common XAFS measurement mode, is schematically represented in Fig. 3a. This is functionally similar to a basic spectrophotometric measurement. However, in contrast to laboratory-scale instruments, synchrotron X-ray sources may be hundreds of metres in diameter and the instrument beamline tens of metres in length. Sample sizes are typically on the order of 1 cm in size, but with suitable focusing instrumentation, the X-ray beam can reach sizes of <1 µm.

X-ray sources

Synchrotron radiation sources. Laboratory-scale XAFS systems using spherically bent focusing crystal monochromators are available commercially and can be useful for concentrated samples and training. More challenging experiments that require higher flux, for example, dilute systems, under in situ or operando conditions, polarization-dependent studies and experiments requiring a well-collimated beam are routinely carried out at synchrotron radiation sources[54]. Synchrotrons are large, shared research facilities, which are normally accessed via a proposal process, offering far more intense and collimated beams of polychromatic and polarized X-rays than laboratory sources. Most of instrumentation necessary to carry out measurements is provided by the facility. At a synchrotron, a recirculating beam of electrons moves through a shielded, evacuated pipe at speeds slightly under the speed of light. The electron beam travels in a closed path (that is, the shape of a many-sided polygon), with rounded corners where the beam path bends. A carefully designed set of focusing quadrupole and sextupole magnets controls the dynamics of the electron beam, and radiofrequency cavities are used to replenish the beam energy lost through synchrotron radiation. The electrons are not uniformly distributed throughout the circumference of the ring, but rather grouped in a number of bunches. For this reason, X-rays are emitted as a train of short pulses, where the duration,

frequency and pattern depend on the operating conditions of the ring. This pulsed structure can be extremely useful for time-resolved and pump-probe experiments.

Accelerating charged particles radiate. Wherever the beam direction is forced to change, for example, by applied magnetic fields, photons are emitted. The relativistic motion of the electrons drastically alters the energy spectrum and spatial distribution of the radiated light, compared with non-relativistic motion. The high-energy end of the spectrum shifts up into the X-ray range, and the emitted radiation pattern tilts and is confined in the direction of electron motion. Normally, the orbital plane of the electrons is horizontal, so the radiation at each bend is emitted in a horizontal fan, of which several milliradians are used for experiments on an individual beamline. The emitted photon beams are highly collimated in the vertical plane, with a very narrow vertical angular spread $\approx 1/\gamma$ radians, typically on the order of 100 µrad, in which γ is the ratio of the electron beam energy to the rest energy of the electron. The emitted photons are used in experiments by sending them down a beamline that has suitable instrumentation, such as monochromators, mirrors and detectors.

In modern synchrotrons, special magnetic structures called insertion devices — including wigglers and undulators — cause the electron beam path to oscillate, usually in the horizontal plane of the ring. X-rays radiated at each oscillation bend are used for experiments. Insertion device characteristics are tailored to specifically produce the spectrum and angular properties needed for experiments. Wigglers, such as bend magnets, produce a fan of radiation several milliradians wide in the horizontal plane and highly collimated in the vertical plane. Collimation in the vertical plane is essential to introduce the photon beam to the beamline optical system. The energy spectra from bend magnets and wigglers are quite broad, with a universal shape characterized by a single parameter: the critical energy E_c. Undulators take advantage of interference effects within the device to collimate the emitted photon beam in the horizontal plane. A pencil beam of photons is emitted, and the energy spectrum bunches into specific energies, peaking at the fundamental energy and its odd-order multiples, with greatly increased intensity at the fundamental and low-order odd harmonics.

There are more than 50 synchrotron sources worldwide, details of which can be seen at lightsources.org. Most of these facilities are third-generation storage rings operating with beam currents up to 400 mA to increase brightness. Efforts have been made to reduce the electron beam emittance for high brightness. Multibend achromat lattices[55] can reduce emittance by one or two orders of magnitude. Fourth-generation storage rings based on the multibend achromat lattice concept have recently been developed (MAXIV, SIRIUS and ESRF), with upgrades planned for several third-generation synchrotrons[56].

Beamlines. Synchrotrons host many beamlines, which operate simultaneously. Beamlines are complex instruments that tailor the properties of the X-ray beam produced from the source. This includes selecting and scanning the X-ray beam energy; rejecting beam harmonics; defining the beam geometry with slits; focusing the beam using X-ray mirrors, bent crystals or other devices; delivering the beam to the sample; amplifying and reading detector outputs; recording detector dark currents and amplifier offsets; documenting and saving data files; and providing a suitable interface to the user. Additionally, beamlines are responsible for protecting experimenters and users from radiation exposure with shielding and user-interlock systems, in addition to protecting hardware from fault conditions. Laboratory XAFS facilities must carry out similar functions.

For XAFS, a narrow slice of the spectrum with an energy width on the order of 1 eV or $\delta E \simeq 2 \times 10^{-4} E$ is selected using an X-ray monochromator. Synchrotron X-ray beams are well collimated in the vertical plane owing to the relativistic motion of electrons in the storage ring. This collimation is advantageous when selecting specific energies using X-ray monochromators. Monochromators usually consist of a sequential pair of flat, highly perfect, crystals made of silicon, germanium or other materials. Only X-ray photons with energy E that are sufficiently close to meeting the Bragg diffraction condition — $n\lambda = 2d\sin(\theta)$, or equivalently $E = \frac{hc}{2d_{hkl}\sin(\theta)}$ — are diffracted by the first crystal. X-ray photons that are not diffracted are absorbed, inelastically scattered or transmitted by the first crystal. The first crystal normally requires cooling by water, helium gas or liquid nitrogen. In this form of Bragg's equation, n is a positive integer, λ is the X-ray wavelength, h is Planck's constant, c is the speed of light and d_{hkl} is the spacing between atomic planes in the crystal that contributes to the diffraction peak designated by hkl. For a given crystal structure, only specific triplets of hkl — for instance, for silicon and germanium 111, 220, 311, 331, 400 — give rise to strong diffraction and are used for the XAFS measurements. When diffracting from the first crystal, the X-rays are deflected by an angle 2θ. A second crystal is placed with diffracting planes parallel to the first crystal, causing the beam to be diffracted parallel to the initial beam direction. This is operationally important because θ is varied over a scan, enabling tuning to different energies so that different absorption edges can be measured and E can be scanned over a 1 keV range to record a full spectrum. Beam control is important to minimize energy drifts[57].

The intensity of the monochromatic X-ray beam is normally monitored using a partially X-ray-transparent detector, such as an ionization chamber, referred to as an ion chamber. This signal is divided out to normalize variations in the detected beam flux. In a transmission mode measurement (Fig. 3a), the beam is directed onto a uniform, partially X-ray transparent sample. The X-ray flux transmitted through the sample is measured using a second ionization chamber. The incident flux I_0 and transmitted flux I are related to the X-ray absorption coefficient μ by $I/I_0 = \exp(-\mu(E)t)$ or $I/I_0 = \exp\left(-[\mu/\rho]_{pe}(E)[\rho t]\right)$, in which t is the path length through the sample and ρ is the sample density. This is the X-ray equivalent of the Beer–Lambert law used in UV–Vis and infrared spectroscopy.

Alternative X-ray facilities. Laboratory XAFS facilities are gaining popularity due to their cost-effectiveness and unlimited availability compared with synchrotron beam time. As access to large-scale infrastructures is limited and highly competitive, laboratory sources are a valuable alternative. Some experiment types such as systems that are toxic or dangerous may not be allowed at a synchrotron but can be studied on laboratory sources[58]. Laboratory set-ups are also valuable as teaching instruments, for example, to explain X-ray methodologies.

A general limitation of laboratory-based experiments is that they have a relatively low signal-to-noise ratio, which needs to be compensated by long acquisition times. As a result, studies of very dilute samples are limited. However, low X-ray doses can be advantageous for samples prone to radiation damage. Time-resolved experiments are also difficult or impossible using laboratory-based spectrometers. Conversely, laboratory XAFS instruments are very interesting for characterizing stable solids and liquids when long-term in situ measurements are required in materials chemistry, catalysts and environmental science. Importantly, laboratory facilities can complement synchrotron studies by performing preliminary measurements for sample screening to maximize synchrotron time. Advances in laboratory-based XAS

will be facilitated by more powerful X-ray sources and highly efficient detectors to reduce acquisition times. As in-house X-ray instruments improve, more X-ray experiments may move back to the laboratory.

XFELs are cutting-edge tools that use high-energy electron beams to produce extremely bright and coherent X-ray pulses. For example, the European XFEL can produce pulses up to 27,000 times per second, enabling real-time observation of rapid processes[59]. XFELs can cover a wide range of X-ray energies to probe various materials and biological samples at different levels. Using an XFEL facility is more complex than a synchrotron; however, they are opening up new perspectives in time-resolved imaging of ultrafast processes in biology and materials under extreme conditions of pressure and temperature[60,61].

Measurement modes

$\mu(E)$ or $[\mu/\rho](E)$ is the central quantity of interest in XAFS. It is analogous to the product of the extinction coefficient and concentration in optical absorption measurements. In transmission mode, absorption from air and windows and the energy dependence of ionization chamber sensitivities add a smooth background to the absorption, which is subtracted later in the data reduction process. In precise fluorescence mode measurements, corrections may be needed to compensate for these effects.

In fluorescence mode (Fig. 3b), X-ray fluorescence emitted from the sample owing to X-ray absorption is measured, rather than the transmitted flux measured in transmission mode. In some situations, it can be helpful to measure both transmission and fluorescence modes at the same time.

Alternatively, with suitable instrumentation, electrons emitted from the sample surface can be used as an indirect measure of the absorption events. This is an important detection approach for low energy, referred to as soft, X-ray energies. Conversion-electron detection can also be effective at higher energies. In this case, electrons emitted by the sample within a depth of ≈1,000 Å are allowed to collide with helium gas around the sample surface, and the secondary electrons are detected with an applied electric field, similar to an ionization chamber. This mode of detection provides a surface sensitivity not automatically possible by other means. Photoluminescence and other indirect measures of absorption can also be used but are not widely supported on beamlines.

Dispersive XAFS measurements are also possible, in which a bent crystal is used to diffract different energy slices of the polychromatic beam into monochromatic beams that impinge on the sample. The different energies can be detected simultaneously, in parallel, using a spatially resolved detector. This approach eliminates the need to scan, which can be useful for time-resolved experiments. Initially, a bent mica crystal was used with photographic film as a detector[62]. Many other XAFS measurement modes are possible and occasionally used. Important examples are oriented samples with polarized X-ray beams, and grazing incidence or total external reflection geometries for surface sensitivity.

Experimental requirements

A strength of XAFS is that it does not require restrictive sample conditions, making it applicable to real-world and in situ experiments. However, there are essential requirements that must be met to obtain good XAFS data. Although standard XAFS spectroscopy is useful for many fields, higher accuracy methods such as X-ray extended range technique (XERT)[63,64] and hybrid[65,66] approaches can attain two orders of magnitude greater sensitivity and accuracy. This is achieved by quantifying systematics and uncertainties, measuring XAFS across extended energy and attenuation ranges and thereby permitting hypothesis testing of structure and theory. Hybrid techniques investigate a wider range of parameters and systematics than a conventional XAFS experiment, but less than an XERT experiment, and are particularly useful for disordered systems, glasses and solutions. Typically, this involves calibration of energy, amplitude, scattering and harmonics, together with characterization of the sample and beam. Guidelines are available for determining precision[67], especially when measuring the variance of repeated measurements under different experimental conditions[68,69].

A set of useful guidelines is contained in the acronym HALO: harmonics, alignment, linearity and offsets. Harmonics should be removed using harmonic-rejecting mirrors, detuning one of the monochromator crystals, or other means, especially for thick transmission samples. The beam should be aligned with the sample and collimated to only see the homogeneous sample and windows between the monitor (I_0) and detector (I). The monitor and detectors should be linear, in the plateau region, and with corrections for any nonlinearities. Systematic offsets, including dark currents, must be monitored and subtracted to compensate for drifts.

Energy range. XAFS requires precise measurements of the data. The magnitude of the fine structure ranges from about 10% of the edge jump in the near-edge region to less than 0.1%. This decreases rapidly above the edge, particularly for systems that are structurally or thermally disordered, and when the central absorbing atoms have neighbouring atoms of low atomic number. EXAFS involves analysis of the oscillatory $\chi(k)$ signal, whose signal-to-noise ratio drops rapidly at high energies. The ability to resolve peaks in r-space owing to contributions from atoms at different distances is usually dependent on the k-range, which is limited by the small signal at high k. For EXAFS analysis, the upper limit of the energy range should exceed $k_{max} > 10–12$ Å^{-1}, which ($E - E_0 \approx 3.8k^2$ eV Å units) corresponds approximately to $E - E_0 > 400–600$ eV and should preferably be twice that. In the soft X-ray range, or the tender X-ray range, sample requirements can be restrictive and may need to be prepared carefully, for example, thin, homogeneous and measured in vacuum.

Energy resolution and sampling. Near the absorption edge, XAFS data may contain sharp peaks and oscillatory features that vary rapidly as a function of energy. Features that vary more slowly versus energy are found further above the edge. This is due to the oscillatory nature of EXAFS versus k, and because $k \propto \sqrt{E - E_0}$. To resolve features near the edge, an X-ray beam of energy bandwidth less than ~1 eV is required. This criterion depends on the core-hole lifetime. If the energy resolution is insufficient, near-edge features will not be resolved, and the EXAFS amplitudes at low k may be suppressed. The trade-off between flux and resolution can be controlled to some extent by the choice of source, crystal cut and slit configuration. The effect of resolution and core-hole lifetime can be partially corrected for numerically, but it is important to use a sufficiently fine instrumental energy resolution and sampling. Typically, energy sampling will be a fraction of 1 eV over the edge, and the energy grid spacing will increase over the EXAFS region to mimic a uniform spacing in k. Some beamline control software will explicitly manage this, and others will require manual selection of energy grids.

Core-hole broadening is a fundamental physical effect that occurs owing to Heisenberg's time–energy uncertainty relation $\Delta E \Delta T \geq \hbar/2$ and the limited lifetime of the core hole. The core hole is annihilated when it is filled by an electron transitioning from a higher energy state. Energy

is emitted in the form of a fluorescence photon. For example, a 1s core hole is quickly filled by a dipole-allowed transition from a 2*p* state, resulting in emission of a *K*-α fluorescence photon. In fluorescence mode, these photons are routinely collected as a measure of the X-ray absorption. For *K*-edges of the first-row transition metals, this happens on a timescale of order 10^{-15} s, giving energy widths of ~1 eV. *K*-edge energy level widths increase rapidly with atomic number, roughly doubling for each 8.75 increase in atomic number of between $Z = 16$ and $Z = 60$. Core holes may also be annihilated through a sequence of non-radiative (Auger) processes in which energy is released by ejecting electrons from the absorbing atom (Fig. 1b). A fraction of these electrons can be detected as an indirect measure of the initial absorption events. *L*-edge hole widths are complex functions of atomic number *Z* (ref. 11).

To adequately represent contributions from the longest effective distances present in the data, it must be sampled on a sufficiently fine grid in energy or *k* and have well-defined accuracy on each data point. The Nyquist sampling theorem suggests that the highest frequency in the data must be sampled at least twice per cycle. The period of EXAFS oscillations in *k*-space satisfies the condition $2\pi = 2\Delta k R_{max}$, so a common Nyquist sampling criterion is $\delta k = \pi/(2R_{max})$, or about 0.16 Å^{-1} for $R_{max} = 10$ Å (refs. 36,67,70). There is also high frequency noise in the data, which can alias into the frequency range of interest and contribute to excess noise if not sampled adequately. For this reason, oversampling is commonly performed. A sampling grid in *k*-space of 0.05 Å^{-1} works well in practice and is recommended for most samples.

Such a sampling convention implies that the spacing between energy grid points E_n in the EXAFS region should satisfy the approximate criterion $\delta E_n \leq \sqrt{(E_n - E_0)/25}$. Oversampling is not a problem; however, undersampling is an issue that can be addressed with well-defined, undersampled data. The undersampled data can achieve exactly the same accuracy and insight as dense data[67] but only if uncertainties and data accuracy are propagated. As a result, there is a danger with perfectly regular spacing, but irregular sampling of component frequencies is potentially highly accurate if uncertainties are measured and propagated.

Samples

Homogeneous concentrated samples can be easily and accurately measured in transmission mode. Films can be prepared by many methods, including evaporation, sputtering, atomic layer deposition and chemical vapour deposition[71]. Thin concentrated films and thick dilute samples can be accurately measured in fluorescence mode. By contrast, thick concentrated samples tend to suffer from self-absorption and over-absorption effects in fluorescence, unless preventive measures are taken.

Sample preparation is a design process, requiring careful thought and execution. Bad sample preparation results in bad measurements. Samples can be made from films, powders, solutions, suspensions or gases. In most cases — nontoxic metal foils are a common exception — samples must be kept in sealed cells with X-ray transparent windows. They can be specifically prepared for XAFS measurements, which is preferred, or analysed in a natural state, which may present challenges. Safety is the first thing to consider, for example, sample toxicity, reactivity, volatility or radioactivity. Safety Data Sheets should be consulted and materials handled accordingly. These considerations affect decisions about sample processing, including grinding, protective equipment, sample cell choice, material transportation and disposal.

The measurement mode used depends on the composition of the sample and its geometrical form. If samples are concentrated and can be prepared with a uniform thickness that is thin enough for the incident X-rays to pass through, then transmission mode measurements are simplest and best. Variations in sample thickness can cause systematic errors, which are exacerbated when the sample is too thick. Thickness effects also occur when the sample is too thin. The best solution is to use multiple samples to quantify and correct for any thickness effects[34–36,72–74].

Sample absorption should be calculated during the experimental design process. If the edge step is small ($\lessapprox 0.1$), then fluorescence mode is preferred. This can be the case if samples are dilute. In such cases, the sample does not need to be thin enough for all X-rays to pass through, because the fluorescence detector can be placed perpendicular to the incident beam. Typically, the beam will be incident on the sample surface at 45°, but other incidence angles can be selected. The fluorescence detector is normally placed at 90° to the incident beam direction in the horizontal plane. This location minimizes elastically scattered background from the sample by aligning the centre of the detector with the X-ray polarization vector of the incident beam.

Equation (11) considers a flat slab of material with thickness *T* and X-ray beam of energy *E* incident at angle θ relative to the sample surface. Fluorescence X-rays of energy E_f exit at an angle ϕ, with $\mu(E)$ representing the absorption coefficient of the whole sample and $\mu_s(E)$ representing absorption only from the element and edge of interest. The fluorescence signal from a layer of sample at depth *t* is the product of several factors: the probability of X-rays propagating to depth *t* ($\exp(-\mu(E)t)$); the probability of being absorbed by the element of interest *s* within the thickness dt ($\mu_s(E)dt/\sin(\theta)$); the probability of an absorption event giving rise to an isotropically emitted fluorescence photon, also known as the fluorescence probability yield *f*, which is a constant between zero and one; and the probability of the fluorescence photon of energy E_f escaping the sample at angle ϕ.

Integrating the product of these probabilities over the thickness of the sample gives:

$$\mu_s(E)\tau(E)(\varepsilon/\sin(\theta))\,(1-\exp(-T/\tau(E))), \tag{11}$$

in which sampling depth or sampling thickness $\tau(E)$ is defined as $1/\tau(E) = (\mu(E)/\sin(\theta) + \mu(E_f)/\sin(\phi))$. $\tau(E)$ is a measure of the depth the X-rays probe the sample in fluorescence yield measurements. The shorter of *T* and τ is the metric to consider if one is much larger than the other.

There are useful limits when equation (11) is expressed in a simpler form. If the total thickness of the sample *T* is much less than the sampling depth ($T \ll \tau$), the expression simplifies to $\mu_s(E)T(\varepsilon/\sin(\theta))$. This is called the thin limit and the fluorescence signal is proportional to $\mu_s(E)$, as desired for direct comparison to transmission mode. Conversely, if the sampling depth $\tau(E)$ is much less than total thickness *T* ($\tau \ll T$), the expression simplifies to $\mu_s(E)\tau(E)(\varepsilon/\sin(\theta))$. This is called the thick limit and the expression has exactly the same form as the thin limit, except the relevant thickness is $\tau(E)$ instead of *T*.

A key difference is that $\tau(E)$ depends on $\mu_s(E)$ because $\mu_s(E)$ is a component of $\mu(E)$. For concentrated samples, this introduces a nonlinear dependence of the measured signal on $\mu_s(E)$ that can distort the XAFS if the element of interest is a major component of the sample. As the sampling depth depends on absorption, it can partially cancel out variations in fluorescence with energy. This effect is referred to as self-absorption or over-absorption and must be minimized with

avoidance procedures or corrected using numerical methods[34–36,75]. Measuring the signal in electron-yield mode instead of fluorescence, collecting fluorescence signal at small ϕ, or using an internal calibration signal — such as fluorescence from lower energy edges, as in the inverse partial fluorescence yield method[76] — can help avoid these problems.

Self-absorption can also occur if particles are not small compared with τ or if the element of interest is not dilute. This can happen even if they are a minor component of a sample that is dilute on average. As a result, particles should be smaller than $\tau(E_a)$, in which E_a is an energy right above the edge of interest.

Apart from the challenge of limited counting statistics, measurements are simpler when the sample is dilute and absorption from the element of interest $\mu_s(E)$ is much less than absorption from the whole sample $\mu(E)$, in other words: $\mu_s \ll \mu$. This is called the dilute limit, which is relevant for systems such as millimolar metalloprotein solutions. In this case, τ is approximately independent of $\mu_s(E)$. The resulting fluorescence signal is again proportional to $\mu_s(E)$, as desired, but now contains a slowly varying energy-dependent factor. This can be easily corrected for, but if ignored will generate small systematic errors in Debye–Waller factor estimates.

Sample preparation. Two essential requirements for transmission samples are that a sufficient fraction of the X-ray photons can pass through the sample and that the variation in absorption from the element of interest is sufficiently large. In practice, this means the total absorption μt of the sample and substrate above the edge should not greatly exceed ~3–4. The edge step, the difference in total absorption $\Delta\mu t$ above and below the edge, should be ~0.5–2.5. Large absorption peaks, referred to as white lines, may occur at the edge in some substances. If these are of interest, the maximum particle size calculation should be based on this maximum absorption coefficient.

The primary concerns related to thickness effects include the presence of uncontrolled non-ideal systematic errors such as residual harmonics in the X-ray beam; scattering around and through the sample; excessive variations in sample thickness; spurious background signals in the upstream monitor (I_0) or transmitted flux detector (I) owing to scattering and fluorescence from other materials in the environment; and tails of the monochromator resolution function. Excessively thick samples harden the X-ray beam, resulting in a greater proportion of residual harmonics. The recommendations described here are a rough guideline. All effects can be mitigated with special care and instrumentation, but this may not be available at a beamline.

Samples for transmission and fluorescence are often films from solid, evaporated, sputtered, electroplated or chemically deposited materials. If they can be made of correct uniform thickness, these are excellent samples. It is also common to make transmission or fluorescence samples from powders. When using powder samples, it is important to ensure that the particle size is considerably less than the absorption length $1/\mu$. This absorption length should be calculated at the energy with the greatest absorption in the range of interest, typically right above the absorption edge. If particles of appropriate size can be precipitated from solution, they are also excellent samples. Otherwise, such materials are typically ground using a mortar and pestle or laboratory mills. Powders are then passed through a sequence of successively finer sieves to select the smallest particles. A useful approximation is that the maximum size particles (in micrometre) that pass through a sieve is 15,000 per mesh — size (in wires per inch). If the required particle size is smaller than available sieves can accommodate, sedimentation in a non-reactive fluid[40] can be a viable procedure. Fine particles that remain suspended in the fluid after a calculated time period are decanted. Once sufficiently fine particles are obtained, they can be applied uniformly to a substrate. Stacking several of these samples can mitigate imperfections from a single foil if the absorption is low. Alternatively, an appropriate amount of the powder can be very thoroughly mixed with a non-reactive substance of low X-ray absorption, such as boron nitride, and made into a pellet of uniform thickness using a laboratory press.

Samples should be inspected visually for spatial thickness variations. Because of the different absorption lengths for visible and X-ray photons, this is not a fail–safe procedure. A useful check is to rotate the film sample in the X-ray beam to vary the X-ray path length through the sample. In transmission measurements, a sample at 45° to the beam should have an absorption $\sqrt{2}$ times that of the sample at normal incidence. Such checks can also reveal the presence of pinholes. Spatial variations in composition and thickness can cause several problems, particularly if the spatial frequency of the variations, for example, striations, is comparable to the spatial frequency of variations in the X-ray beam, such as apertures, mirror structures or interference owing to partial coherence. Crystal glitches are aberrations in the angle versus energy of the X-ray beam that occur when multiple sets of crystal planes in the monochromator simultaneously satisfy the Bragg condition. These can be mitigated by suitable choice and orientation of monochromator crystals. Such variations also strongly couple into sample inhomogeneities.

It is always a good idea to run a blank sample in fluorescence measurements. The blank should be known not to contain the element of interest. This is because fluorescence of the element of interest can often be detected from a material in the sample environment excited by scattered X-rays rather than from the sample itself.

X-ray beams are normally linearly polarized. If the angular distribution of crystallites in a sample is not isotropic and the crystallites are not randomly oriented, for example, if they are partially ordered by compression, care must be taken to either eliminate the effect or to account for it in data analysis. Magic angle spinning[40] can average out this undesired X-ray linear dichroism.

Radiation damage is a concern for all materials, especially for aqueous samples such as metalloprotein solutions. The effect on spectra can be mitigated by flash-freezing samples to reduce the mobility of hydrated electrons and free radicals, but the damage can still occur. Radiation damage can be monitored visually, with spectrometry, or by monitoring the time dependence of XAFS spectra. This can introduce sample inhomogeneities in a normally homogeneous sample. A common way to manage these problems is to change samples by translating or rastering through the X-ray beam, so that fresh spots are illuminated. Alternatively, the sample can be flowed through the X-ray beam. For some materials, X-ray-induced decomposition of the sample can introduce a reactivity hazard.

Effects of sample thickness variations in transmission. Homogeneity of sample thickness and composition is important for transmission XAFS measurements. Inhomogeneous samples give rise to noisy and distorted spectra, resulting in incorrect EXAFS amplitudes and XANES interpretations. The basic equation $I/I_0 = \exp(-\mu(E)x)$ assumes that thickness x is uniform. Real samples are imperfect and thickness variations must be considered[40,77]. Variations in thickness x of the sample can be characterized by a probability distribution $P(x)$. This implies that $(\mu x)_{\text{measured}} = -\ln(\int_0^\infty P(x)\exp(-\mu x))\mathrm{d}x$. If the mass attenuation coefficient, also defined as the cross-section per unit mass, is used to

describe the absorption, then $P(x)$ describes the variation in mass thickness. This is the integral of the material mass density over the X-ray path through the sample, which varies across the beam footprint. This integral has a form that defines the cumulant expansion, giving for any distribution:

$$(\mu x)_{\text{measured}} = -\sum_{n=1}^{\infty} \frac{C_n}{n!}(-\mu)^n \approx C_1\,\mu - C_2\,\mu^2/2 + C_3\,\mu^3/6 - \ldots, \qquad (12)$$

in which the C_n are the cumulants of the thickness distribution. For a Gaussian distribution, only C_1 and C_2 are nonzero. C_1 and C_2, respectively, represent the mean value $\bar{x}$ and variance σ_x^2 of the thickness distribution $P(x)$, whereas C_3 relates to the skewness of the distribution and C_4 the weighting in the tails of the distribution relative to a Gaussian distribution of the same width σ_x. A simple recursion relation connecting power moments and cumulants was derived in ref. 29 and can be found in ref. 40.

As C_2 is intrinsically positive, the form of equation (12) indicates that variations in thickness always tend to suppress the apparent measured absorption $(\mu x)_{\text{measured}}$. These variations are more pronounced for larger $\mu(E)$. An extreme case of this occurs in the presence of pinholes — small areas with zero thickness — which should be avoided at all costs.

Nonlinear detector and electronics chain response

It is important that the detector response is linear. For all sources of nonlinear response, suitable corrections must be made to make the detector chain linear. This means that if the detected number of photons is doubled, the signal should also precisely double. Pulse counting detectors have inherently limited count rates associated with dead times. Dead-time corrections are standard and should always be done. They are sometimes built into the detector electronics. When using pulse-counting detectors, the repetition rate of the X-ray pulses from the ring also imposes a rate limit. The time responses of the detector and electronic systems for the reference (I_0) and signal (I) should be matched for best results.

The ionization chambers must be operated in their plateau region where effectively all of the electron–ion pairs are collected before they have time to recombine. If the ionization chamber voltage is too low, recombination will occur and the measured signal will not reflect the actual absorbed power. If the voltage is too high, amplification will occur. This is because the charges in between collisions can be accelerated to energies high enough for secondary ionization, essentially turning the ionization chamber into a proportional counter. The voltage required depends on the plate spacing, type of fill gas and total intensity and spatial distribution of the X-ray beam, which gives rise to space charge within the fill gas. Operationally, the plateau region can be determined by increasing the voltage on the ionization chamber at a fixed flux until the current no longer increases. This is the plateau region of the voltage curve and the measurements should be made with a voltage exceeding it.

There is a common misconception that by using identical detectors with identical voltages and fill gases, the nonlinearities will cancel out. This can be shown to be incorrect. The detector response can be considered as a function of signal S, denoted $R(S)$. It is necessary that $R(0) = 0$, which means that there is no output with no signal in. In practice, this is routinely performed at beamlines by using the data acquisition software to accurately measure and then subtract the amplifier offset voltages and detector dark currents from the recorded data. Small positive current-amplifier offset voltages are actually desirable as they enable current amplifiers to operate in their most linear ranges; however, they must be subtracted out.

The goal is to determine the ratios of signals S_1 and S_0 from their measured responses $R(S_1)/R(S_0)$. This compensates for variations in the incident beam intensity. If the detectors are linear, and offsets and dark currents are subtracted out, then $R(S) = \alpha S$ in which α is some non-zero constant. In this case, the desired situation is $R(S_1)/R(S_0) = \alpha S_1/(\alpha S_0) = S_1/S_0$. However, with nonlinear detectors, $R(S)$ can be expanded as a Taylor series in the signal S as $R(S) \approx \alpha_1 S + \alpha_2 S^2 + \alpha_3 S^3 \ldots$. Then $R(S_1)/R(S_0) \approx S_1/S_0 + (\alpha_2/\alpha_1)(S_1 - S_0) + \ldots$, and the relative error to leading order is $(\alpha_2/\alpha_1)(S_1 - S_0)$. This is not zero unless S_1 and S_0 are equal, which is generally not the case. If the signals could be kept sufficiently close in magnitude over the course of a scan, the effect could be mitigated, but signals in the downstream I chamber change substantially as the energy passes over an absorption edge, whereas the signal in the reference I_0 chamber does not. This systematic error persists whenever the detectors are nonlinear, even if they have identical response curves. At minimum, this will produce EXAFS normalization errors, and possibly worse, depending on the extent of the nonlinearity.

A better procedure is to quantitatively measure detector nonlinearities and apply corrections (the inverse function $R^{-1}(S)$) to the signals if needed. This is relatively straightforward and can be integrated into beamline software, or applied to recorded data after the fact. The procedure used is to systematically attenuate the beam, for example, by narrowing slits, until a linear response is achieved. The nonlinear $R(S)$ function and its inverse function $S(R)$ can then be determined. A suitably de-noised version of this empirical function can be applied to the measured data to linearize it. This procedure has been successively used for dead-time corrections of pulse counting detectors. If the detector system is sufficiently linear, such as by plateauing the ionization chambers and matching time constants of electronics, then corrections may not be needed, however, this should be verified.

Using nonlinear detection systems without appropriate corrections increases noise and artefacts in the data owing to natural variations in beam intensity and crystal glitches. This can distort features in the data and EXAFS amplitudes. Correcting the nonlinearity largely corrects these problems (see ref. 78).

Dilute systems

When samples are dilute, the signal-to-noise ratio is driven by the limited number of collected signal fluorescence photons and background photons, both of which fluctuate. The background can be from elastic and inelastic scattering from the sample, fluorescence from other elements in the sample or other sources. The Poissonian fluctuations in the number of photons vary as $\sqrt{N_{\text{tot}}}$, in which $N_{\text{tot}} = N_s + N_b$, and N_s is the number of signal (fluorescence) photons acquired in a specific time interval and N_b is the number of background photons. The signal-to-noise ratio then is $S/N = N_s/\sqrt{N_s + N_b} = \sqrt{N_{\text{eff}}}$, in which N_{eff} is the number of effective counts. If there were no background and N_{eff} counts, the S/N ratio would be the same as if there were N_s signal and N_b background counts: $N_{\text{eff}} = N_s^2/(N_s + N_b) = N_s/(1 + (N_b/N_s))$. This useful expression shows that the presence of background can diminish the effective counts by the background-to-signal ratio. For dilute systems, it becomes imperative to eliminate the scattered background.

In fluorescence mode, the desired signal is entirely at the fluorescence energy E_f, whereas elastically scattered background photons are at the higher and variable energy of the incident beam and inelastically scattered X-rays are at a slightly lower energy. Placing the window of an energy-resolving detector to accept a narrow region around the

fluorescence energy can be an effective way to exclude background if the detectors can handle the count rates. Multi-element germanium and silicon drift detectors are commonly used for this purpose. In some cases, it can be helpful to use Lytle or Stern–Heald-type detectors with $Z-1$ filters and Soller slits or diffractive analysers[79–81] to reduce the background before it gets to the detector.

It can be beneficial to use N_{eff} as an optimization tool in dilute fluorescence measurements. The signal can be taken as proportional to the edge jump, which is the signal above the edge A minus the signal below the edge B, without needing to convert measured signals to photon equivalents, $N_{eff} \propto (A-B)^2/A$. Varying experimental conditions — detector placement, presence and type of filters and type and location of slits — to maximize $(A-B)^2/A$ provides a simple metric for manual or automatic optimization.

Results

The XAS spectrum is typically divided into the XANES and EXAFS regions. In the near-edge region, electron transitions may occur to unfilled bound states, nearly bound states (resonances) or continuum states of the appropriate symmetry, whereas in the EXAFS regions transitions are to the continuum. It is understood that the physical processes that define both regions are the same, but the distinction is used to ease the data analysis. By adopting some simplifying approximations, it is possible to perform a full quantitative analysis of the EXAFS region, although this is currently not generally the case for the XANES part of the spectrum, in which most of the analysis is still performed semi-quantitatively or qualitatively. Despite the challenges associated with comprehensive analysis of the XANES region, measurements in this spectral range have the advantage that they can be performed at lower concentrations, in less-than-perfect sample conditions, and can be collected very quickly, enabling time-resolved experiments.

XANES

As a rule of thumb, the XANES region covers the lower energy portion of the absorption spectrum starting just below and up to ~30 eV above the absorption edge (Fig. 1). This is a region where multiple scattering processes are important. Multiple scattering is when the ejected photoelectron is scattered sequentially by more than one neighbouring atom before returning to the absorbing atom. Here, the photoelectron scatters from one atom (single scattering, two-leg paths) to another atom (double scattering, three-leg paths) and then returns to the initial site of photoabsorption, because the inelastic losses are relatively weak. The XANES region includes the rising edge, containing both the threshold to ionization and higher energy bond states, as well as pre-edge features, which correspond to transitions to bound unfilled orbitals. It contains information about the electronic structure of the absorbing atom (oxidation state and density of states), coordination symmetry (tetrahedron and octahedron) and orbital occupancy.

Until recently, XANES analysis was largely performed by simple fingerprinting to compare the measured features of the sample with the spectra of known model compounds. The energy position of the absorption edge was traditionally used to estimate the formal valence state of the absorbing atom. The bond length of atoms that coordinate to the absorbing atom also affects the edge position[40,82]. In addition, some features in the rising edge, such as the resonant transitions, can infer information about metal–ligand overlap[83–86]. Additionally, the energy position, shape and intensity of the generally weak pre-edge features can empirically determine orbital hybridization, ligand field and local coordination symmetry[86–90].

Within the fingerprinting approach, linear component analysis or linear composition fitting is commonly used to interpret XANES spectra and elucidate the ratios of valence states or phases[91,92]. In these cases, it is important that the model compound spectra accurately represent components in the unknown sample. Ideally, these standards should be measured under similar experimental conditions and processed identically to the unknown sample spectrum. Model compounds, such as metal foils or other crystalline samples with long-range order, are not be well suited to derive the composition of samples with no long-range order or when the disorder is large. When investigating the chemical composition of a series of spectra taken as a time sequence of a chemical reaction, a good strategy is to use the spectra of the product and reactant as selected model compounds.

More sophisticated linear algebra techniques can be used to interpret XANES spectra, such as principal component analysis[93,94]. Using these approaches, there is no requirement for model compounds, but the analysis will only provide the number of significant components that contribute to the overall set of collected XANES spectra. This is especially powerful when analysing XANES spectra in a time series, as it enables the presence of a reaction intermediate to be determined. Other chemometric approaches, such as multivariate curve resolution-alternating least square (MCR-ALS) algorithms[95–97], can also be used for XANES interpretation. Using a set of constraints, the MCR-ALS approach intends to disentangle the XANES spectra of the pure species and estimates their contribution to each spectrum in a series. Although no prior chemical information is needed, some constraints are used during optimization to provide chemically relevant output. These constraints include non-negativity of the spectra, unimodality of the concentration profiles and a constant total concentration of the absorbing species.

Traditionally, XANES data analysis was limited to qualitative techniques; however, this has changed in the past decade[98]. The development and implementation of more accurate and computationally efficient codes, alongside more powerful computing infrastructure, means that XANES spectra can be simulated with a wide variety of methods, at different complexity levels depending on the system and structural model.

X-ray absorption spectra described by the atomic multiplet theory is appealing as the method is extremely computationally efficient. Atomic multiplet theory[99], implemented in software such as Quanty[100], works well to describe features in localized states such as d-orbitals at the $L_{2,3}$-edges. The code is suited to studying open-shell systems and when the core hole contains an orbital moment. Multiple scattering theory, which is available in CONTINUUM[101], FEFF[102] and MXAN[103,104], can efficiently use a Green function formulation of the XAS problem. Increasing computational complexity, the finite difference method (FDM) implemented in FDMNES[105,106], enables the simulation of the XANES spectrum beyond the muffin-tin approximation. These codes can be used for XANES simulations of large molecular, crystalline or low-dimensional systems, but an input structure is needed. Electronic structure simulations based on density functional theory (DFT) as implemented in Quantum ESPRESSO[107] and molecular dynamics simulations, for example, in VASP[108,109], provide a platform for simulating the XANES spectra of electronic transitions; however, they heavily rely on approximations such as the core-hole and interatomic potential approximations. These codes often use the plane wave pseudopotential method, making them suited for simulating ordered crystalline systems.

Beyond DFT, explicit calculation of core electron excitations by time-dependent DFT[110] is possible in codes such as FDMNES[106,111],

ORCA[112], ADF[113] and FDMX[114], which are widely used to interpret pre-edge features in the XANES spectrum. These codes are quantum chemistry or quantum physics software packages that perform simulations using localized basis sets in open boundary conditions. As a result, they are useful for simulating molecules, clusters and nanoparticles. In addition, many-body effects such as local fields and core-hole interactions, which are necessary to describe excitonic effects, are now estimated in some advanced codes. OCEAN[115–117] and Exciting[118] use a two-particle 'Bethe–Salpeter' equation approach to many-body effects, although this often requires greater computational complexity. A comprehensive description of these codes can be found in ref. 43.

Future codes for exchange and non-locality will be needed for many-body effects and accurate spectra. However, even the most advanced computational approaches have problems with the accuracy and reliability of simulations. In addition, none of the codes currently delivers the three pillars of practical user accessibility: wide and general applicability, reasonable computational cost and user friendliness. Consequently, most advanced XANES analysis is performed by highly focused subject specialists. Several initiatives to lower the access barrier to these codes are being developed, such as Web-CONEXS[119], which aim to provide a user-friendly web application to mitigate the difficulties of ab initio simulations by interfacing codes frequently used for XANES simulations (ORCA, FDMNES and Quantum Expresso) with an established high-performance computing facility.

EXAFS

The EXAFS region, beginning around 30 eV above the absorption threshold and extending for hundreds of electron volts, is the oscillatory structure that modulates the absorption spectrum[31]. The EXAFS function $\chi(k)$ is usually fitted and analysed. Some packages simultaneously fit $\chi(k)$, $k^2\chi(k)$, $k^3\chi(k)$ and $\chi(r)$, although there are theoretical challenges with this. Commonly, a Fourier transform (FT) is used to model and analyse the spectrum into R space, $\chi(r)$ versus r, to show radial density functionals $\chi(r)$. By filtering and back-transforming, the spectrum can be converted into Q space to fit $\chi(q)$ versus k. Theoretical codes such as FEFF[120], GNXAS[121] and EXCURVE[122] were traditionally used to calculate the theoretical spectrum, which is then fit to the experimental data. With the advent of packages such as FDMX[114], fitting can be performed directly in E space as $[\mu/\rho](E)$, $[\mu/\rho]_{pe}(E)$, $\mu(E)$ or $\mu_{pe}(E)$ versus E, including fitting of the near-edge, XANES and pre-edge[98,114,123]. Statistical analysis should be performed to estimate the confidence limit of each determined parameter.

When attempting an EXAFS analysis, a theoretical model of the system of interest is constructed, including the unknown parameters to be determined in the model optimization process. Some fitting parameters are highly correlated, as they affect the amplitude or the phase in a similar or even identical manner, see equation (6). For example, S_0^2 and N_j are both multiplicative factors that scale the amplitude of the EXAFS signal and have a 100% correlation coefficient. σ_j^2 also affects the signal amplitude, with a dependency that is exponential instead of linear. These parameters can be fit together, although it is important to remember that they are highly correlated. R_j and E_0 are also highly correlated as they both affect the phase, or offset, of the EXAFS signal.

The oscillatory structure of the EXAFS signal is due to interference between the ejected photoelectron wave and photoelectron waves backscattered by neighbouring atoms. As a result, the EXAFS signal contains detailed structural information around the absorbing centre, including nature of the coordinating atoms, coordination numbers, bond lengths and order/disorder. The basic theory governing the EXAFS spectrum is relatively well understood[1,15,111,117,124], and quantitative analysis is routinely performed. The EXAFS signal is the sum of the contributions of each electron orbital in each individual scattering atom, j; or single and multiple scattering from the full potential of the full electron density of the material. In the EXAFS equation, N_j (coordination number), R_j (interatomic distances) and σ_j^2 (the root mean square fluctuation in bond length) are fitted structural parameters, together with S_0^2, the amplitude reduction factor that accounts for inelastic losses, and E_0. Normally, $|f_{eff}|$, $\delta_j(k)^l$, Φ_{eff} and $\lambda(k)$ are predicted from theory; however, there are notable variations and future advances in theory are expected[11].

EXAFS data reduction. Before analysing the EXAFS structure, $\chi(k)$ is conventionally isolated from the experimental attenuation data. The steps to achieve this are described in ref. 125 and illustrated in Fig. 4. The first step involves subtracting a smooth pre-edge function from the experimental $\mu(E)$ or ideally $[\mu/\rho]_{pe}[\rho t](E)$. The function is usually approximated by a Victoreen or exponential function and calculated by extrapolating the pre-edge region of the data (yellow line in Fig. 4a). This attempts to account for instrumental background and absorption from other edges. Most packages require this step (Fig. 4a).

The second step is to define and fit the energy of the edge E_0. This is often defined as the energy value where the first derivative reaches a maximum in the absorption signal, which is neither the fitting value E_0 nor the Fermi level E_0 from theory. This value of E_0 is then used to estimate the photoelectron wavenumber k. Most packages require this as a fitting parameter. Following the definition of E_0 and k, the data $\mu(E)$ are normalized so that the edge jump is set to one and is dimensionless (Fig. 4b). This is performed so that the resulting spectrum represents the absorption of one atom and is intended to compensate for differences in the thickness or concentration of a sample. It is usually achieved by dividing the experimental spectrum by the edge jump. This step can be avoided in optimized packages and analysis.

The final step removes a smooth post-edge background function (Fig. 4a,b), so that $\chi(k)$ versus k can be extracted (Fig. 4c). This step is intended to remove external sources of slow variation in the signal, such as the energy-dependent detector sensitivity (see red line, Fig. 4b). This should not remove any oscillatory information from the EXAFS data and should only remove the very low frequency components, referred to as the true reference background[126]. Ideally, the subtracted background approximates the absorption of an isolated atom $\mu_0(E)$. This is the most challenging step, as the choice of an optimal background function is not trivial.

Some packages routinely transform the χ versus k data into $k^2\chi$ versus k, before taking FTs of χ or $k^2\chi$ versus R into R-space for fitting. FTs are often used qualitatively to obtain information on the coordination environment of the photoabsorber atom or to compare different systems. However, the amplitude, shape and resolution of FTs largely depend on the k range and window used in the transform, as seen in Fig. 4d–f. EXAFS data reduction is relatively straightforward and is often performed in a semi-automated manner[127]. Discussion of χ extraction and particular issues can be found in ref. 128.

EXAFS data analysis. Figure 5 presents an example of data analysis and fitting. Many popular EXAFS fitting programmes use a conventional, Levenberg–Marquardt nonlinear minimization algorithm. This involves minimizing the difference between the theoretical model and experimental data for each data point $(i, E_i, k_i, [\mu/\rho][\rho t]_{pe}(E_i), \chi(k_i))$.

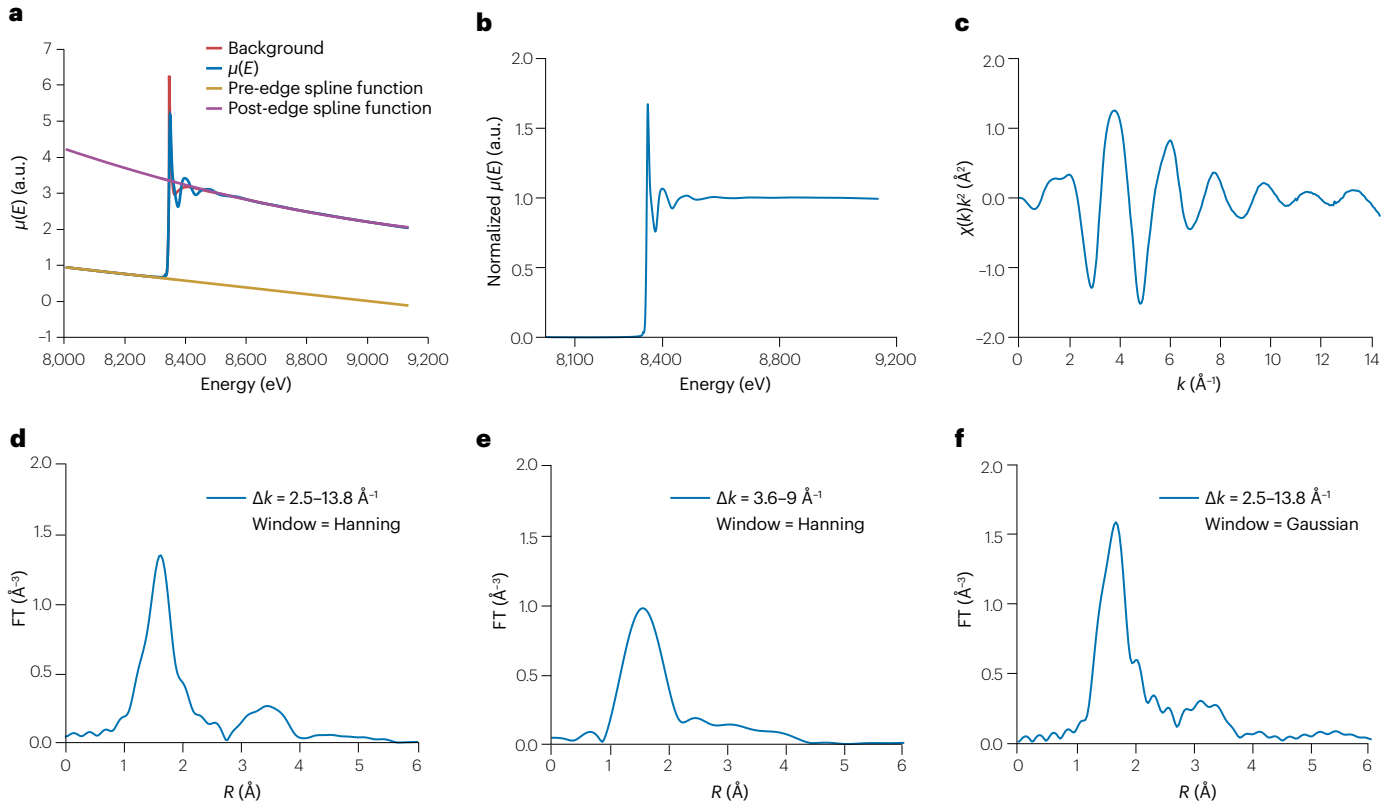

Fig. 4 | Example normalization and extraction of an extended X-ray absorption fine structure spectrum from the raw X-ray absorption spectroscopy data. a–**c**, A linear background function (yellow line) is subtracted from the pre-edge region of the X-ray absorption spectroscopy spectrum, whereas a post-edge fitting curve is subtracted at high energy (purple line) to obtain the normalized spectrum after dividing for the edge jump (panel **b**). The red curve in panel **a** represents the spline function subtracted from the post-edge region to obtain the $\chi(k)$ extended X-ray absorption fine structure spectrum (panel **c**). **d**–**f**, Fast Fourier transforms of the $k^2\chi(k)$ signal representing the non-phase-shift-corrected distance distribution of the backscattering atoms from the photoabsorber, but depend on the scaling with χ and the range of the transform. **d**, Common range for the transform showing two sets of atoms in the structure. **e**, Relatively narrow range of data to be transformed, showing the loss of information on the second shell of atoms, and relatively high noise. **f**, A different window function used before transform, which introduces a fictitious oscillation of electron density in the transform. a.u., arbitrary units; FT, Fourier transform.

The reduced χ^2 parameter, χ_r^2, is defined as the fitting metric χ^2 normalized by the number of degrees of freedom, in other words, the difference between the number of independent data points and the number of fitting parameters used. The χ_r^2 is a useful parameter when comparing several fits. If adding additional variables reduces χ_r^2, there is confidence that the resulting fit may have been improved. In principle, this permits hypothesis testing to distinguish a correct or improved structural model or parameter from an incorrect or less adequate model.

A good fit would ideally have a value of χ_r^2 approximately 1 or less, indicating that the difference between the fit and the model is within the experimental uncertainties. However, in reality, the values of χ_r^2 are usually much larger than 1. This is due to estimation of ε_i and common inappropriate formulae used for χ_r^2. In most cases, it is assumed that the noise is dominated by counting statistics. Very few examples can be found in which other sources of random noise, such as nonlinear response of instrumentation or electronic noise, are considered. Major systematic errors of measurement should also be taken into consideration[63,129].

For a discussion of Nyquist, χ^2, χ_r^2, the number of independent data points N_{idp} and the number of independent fitted parameters N_{par}, see refs. 36,70. In brief, these should be defined as:

$$\chi_r^2 = \frac{\chi^2}{N_{idp} - N_{par}}, \tag{13}$$

in which the fit might have N_{idp} ~ 122 and N_{par} ~ 4. Equally:

$$\chi^2 = \sum_{i=1}^{N_{idp}} \frac{\left(y_i - f(x_i)\right)^2}{\sigma_i^2}, \tag{14}$$

in which $f(x_i)$ is the fitting function for the data x_i, and y_i is the experimental datum, both in units of $\chi(k)$ and both in k space, although this is not always the case in common packages. It is also important that reasonable or accurate estimates of the data point uncertainty σ_i are used for each data point. Without these estimates, the parameter uncertainties and χ_r^2 values will be far from unity, severely constraining the ability for hypothesis testing. In some texts and packages, ε_i is used instead of σ_i, although usually with a different meaning.

An additional parameter often used to determine how close the fit is to the experimental data is the R-factor, which is the fractional

difference between the experimental and theoretical EXAFS functions over the experimental EXAFS.

Although the described parameters can achieve the best statistically valid fit, they do not guarantee that the result is a good fit, namely, that it has physical meaning. There are specific guidelines on the plausibility of some fitting parameters that should be followed when analysing the EXAFS data. S_0^2 should be in the range of 0.8–1.0 (ref. 130) or 0.7–1.0 (ref. 131) and should not be larger than 1 within, for example, three standard errors of uncertainty. The fitted R_j should not result in non-physical bond lengths; they should neither be too short or too long. σ_j^2 should always be positive. General outer shell j parameters should have larger σ_j^2 than inner shells, both due to increased path length and increased disorder for non-crystalline systems and imperfect crystals. The change in E_0 should ideally only be a few electronvolts from the correct Fermi level, not necessarily from the experimental derivative extremum or the arbitrarily defined offset[67,132,133].

For disordered systems, such as liquids, glasses, nanoparticles and amorphous materials, the distribution of atoms around the photoabsorber is not Gaussian in shape. Asymmetric shells must be used to correctly analyse the experimental spectra. Using Gaussian distributions in the analysis of highly disordered systems leads to systematic errors in distances and Debye–Waller factors[134]. Different approaches can account for asymmetry in the distributions, such as cumulant expansion, Γ-like functions or external structural models from molecular dynamics simulations or reverse Monte Carlo approaches[135–138].

Applications

XAFS is a powerful tool for acquiring short-range structural information about the environment of a given photoabsorbing atom with picometre sensitivity. It is also the method of choice to determine the oxidation state of any element and is applicable to samples in any aggregation state. These characteristics mean that XAFS can be applied to a wide range of systems and diverse scientific fields. XAFS is most useful when quantitative detail is required, either as a standalone technique or combined with other spectroscopic probes or theoretical approaches. Areas where XAFS is increasingly common include chemical, biological and physical sciences, with widespread use in catalysis, battery research, semiconductors, materials science, electrochemistry, geochemistry, condensed matter physics and structural biology. Major applications are also in fundamental studies looking at static and dynamic disorder, inelastic mean free paths, plasmons, photoexcitation processes, magnetic materials, surfaces and interfaces[139]. This section provides some examples of scientific questions that XAFS can answer. Figure 6 presents five typical applications of XAFS and the insights that it can provide. Table 1 summarizes a range of applications across different fields.

Chemical sciences

Applying XAFS to catalytic systems, both in the homogeneous and in the heterogeneous phases, enables quantitative analysis of the chemical properties of the active species involved in the transformation. In transition metal-based catalysis, operando XAFS experiments are used to gain information on the spin, oxidation and structural states of intermediates during the catalytic cycle. The large number of XAFS spectra acquired during operando experiments may be further analysed with multivariate statistics and theoretical modelling. In heterogeneous catalysis, XAFS has been applied to various systems, such as iron-based and copper-based zeolites[140,141], supported single-atom catalysts[142] and high-entropy oxides active towards low-temperature CO oxidation[143]. XAFS can study copper speciation in copper-zeolites, for example, copper-exchanged zeolites with chabazite topology (Cu-CHA)[141,144], and copper-mordenite (Cu-MOR)[145–149], which can stabilize Cu-oxo species to directly convert methane to methanol, and ammonia-mediated selective catalytic reduction of harmful nitrogen oxides (NH_3-SCR)[150–154].

Reaction mechanisms involving organic substrates in solution on the second-to-millisecond timescales can be investigated by XAFS. This information is especially valuable when labile and short-lived reaction intermediates or if species difficult to detect with conventional methods are involved, such as the Zn(II) cation. For instance, XAS was applied to reactions involving non-haeme iron complexes active towards C–H oxidation[155–158] and reactions of terpyridine-based copper[159] and zinc[160] coordination complexes. By using XAFS, the number, nature, concentration–time evolution and structure of the relevant reaction intermediates could be quantitatively determined.

XAFS has been successfully used in energy storage and electrocatalysis. For example, XAS elucidated the structure and function of an amorphous cobalt sulfide (CoS_x) catalyst active towards the hydrogen evolution reaction. Ex situ and operando measurements

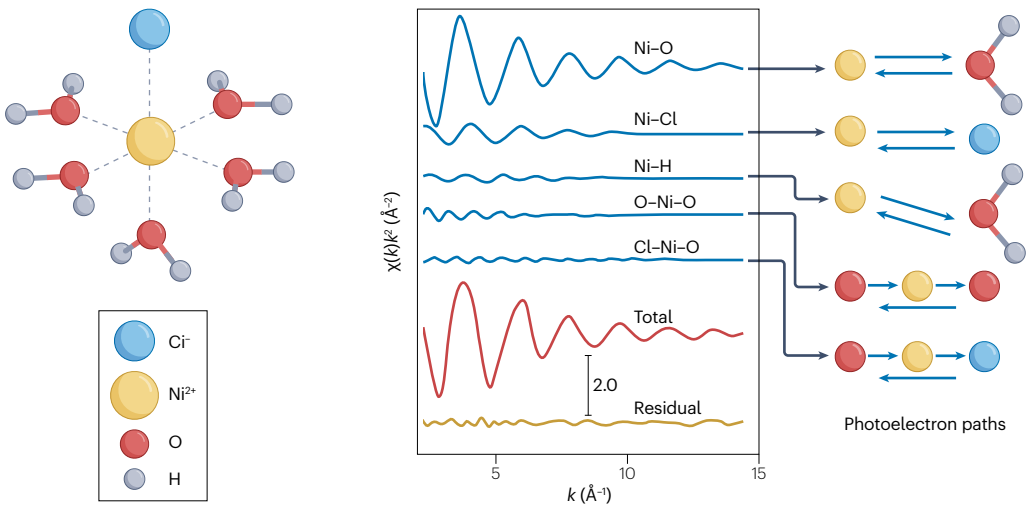

Fig. 5 | Data analysis of the extended X-ray absorption fine structure spectrum of the $[NiCl(H_2O_5)]^+$ cluster. A total theoretical signal is calculated including the Ni–O, Ni–Cl and Ni–H two-body single scattering paths and the O–Ni–O and the O–Ni–Cl three-body multiple scattering paths. The total theoretical signal (blue line) is compared with the experimental $\chi(k)$ spectrum (red line). The agreement is excellent, evidenced by the residual curve (yellow line).

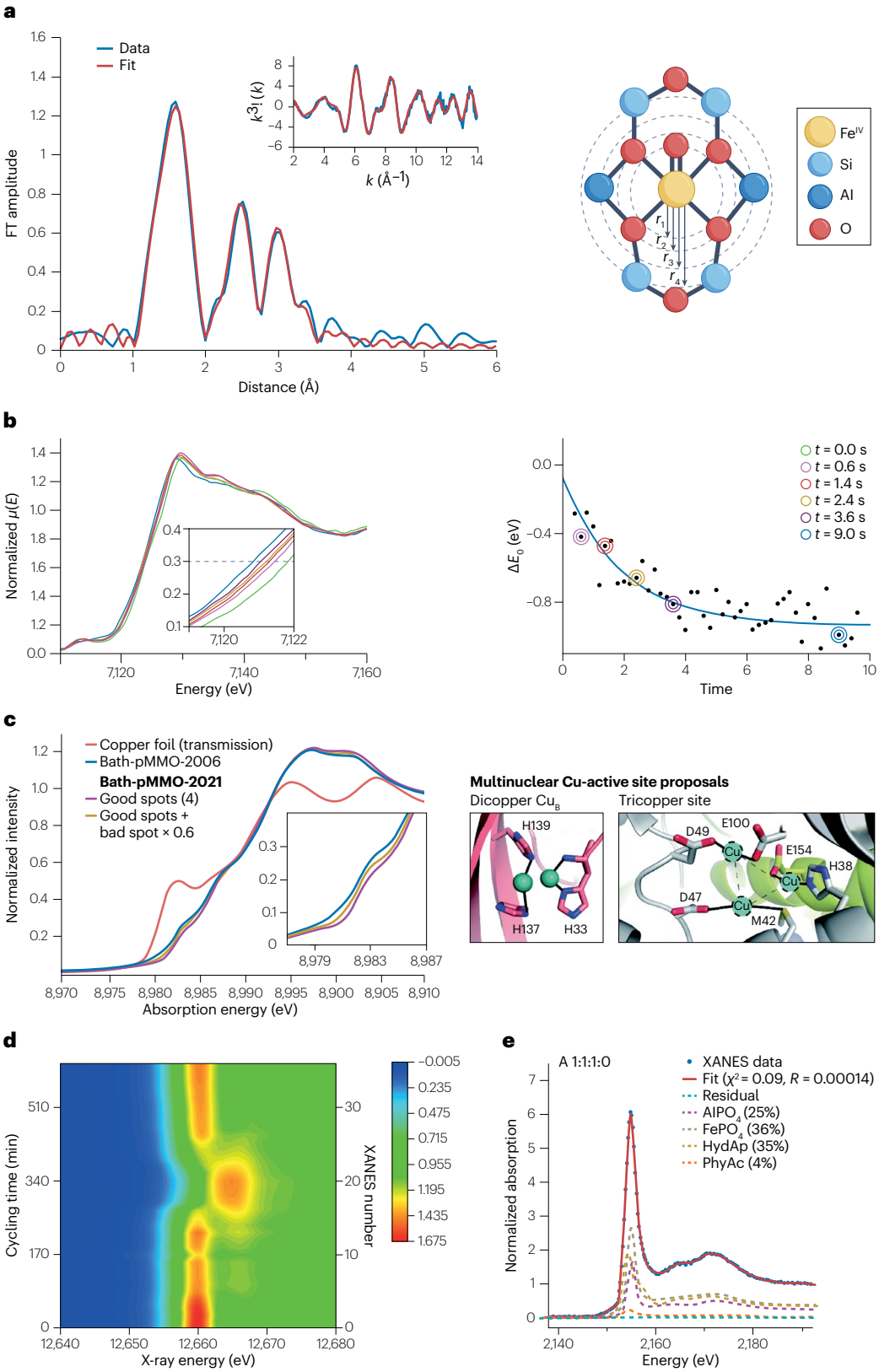
a
Data
Fit
FT amplitude
Distance (Å)
$k^3\chi(k)$
k (Å^{-1})
r_1
r_2
r_3
r_4
Fe^{IV}
Si
Al
O
b
Normalized $\mu(E)$
Energy (eV)
ΔE_0 (eV)
Time
t = 0.0 s
t = 0.6 s
t = 1.4 s
t = 2.4 s
t = 3.6 s
t = 9.0 s
c
Copper foil (transmission)
Bath-pMMO-2006
Bath-pMMO-2021
Good spots (4)
Good spots + bad spot × 0.6
Normalized intensity
Absorption energy (eV)
Multinuclear Cu-active site proposals
Dicopper Cu$_B$
Tricopper site
H139
H137
H33
D49
E100
E154
H38
D47
M42
Cu
d
Cycling time (min)
XANES number
X-ray energy (eV)
e
A 1:1:1:0
XANES data
Fit (χ^2 = 0.09, R = 0.00014)
Residual
AlPO$_4$ (25%)
FePO$_4$ (36%)
HydAp (35%)
PhyAc (4%)
Normalized absorption
Energy (eV)

Fig. 6 | Example applications. a, Fe^{IV}-active site structure in an iron-beta zeolite (BEA) capable of hydroxylating methane. Left: Fourier transform (FT) of the extended X-ray absorption fine structure (EXAFS) and the best-fit result. EXAFS signals are compared in the inset. Right: structural model of the Fe^{IV}-active site in Fe-BEA. Dashed circumferences highlight different coordination shells. **b**, Reaction of methyl-phenyl-thioether (PhSMe) with the oxidizing complex $[N4Py{\cdot}Fe^{IV}(O)]^{2+}$ to produce methyl-phenyl-sulfoxide and $[N4Py{\cdot}Fe^{II}(O)]^{2+}$. Left: time evolution of iron *K*-edge X-ray absorption spectroscopy (XAS) during the reaction, showing reduction of the complex. Inset: the iron *K*-edge region. Right: time evolution of the energy difference ΔE_0 between the iron *K*-edge at time *t* and at time $t = 0$ s. Blue: first-order kinetic fit of experiment. **c**, Copper-active site in particulate methane monoxygenases (pMMO). Left: copper *K*-edge PFY spectra of a copper foil (red) and different pMMO sample spots (purple, yellow curves) compared with previous data (blue curve). Right: proposed models for the multinuclear copper-active site in pMMO. The structural information from EXAFS led to a proposed mononuclear copper-active site for pMMO, solving literature discrepancies. This highlighted how radiation damage in biological samples gives rise to spectral features hampering the determination of structural parameters. **d**, In situ investigation of delithiation in Li/SeSx batteries. Contour plot of the selenium *K*-edge XAS evolution during cell cycling. Combining the structural and electronic information provided by XAS with information from high-energy resolution fluorescence detection pinpointed the selenium speciation throughout the cell cycling. **e**, A protocol for soil phosphorus speciation analysis via phosphorous *K*-edge X-ray absorption near-edge structure (XANES). Linear combination fitting of XANES collected on a mixture of $AlPO_4$, $FePO_4$, hydroxyapatite (HydAp) and phytic acid (PhyAc) showing the difference between experimental data and the best-fit result. Linear combination fitting protocols can determine the phase composition of real samples even if components are amorphous. Part **a** reprinted with permission from ref. 140, National Academy of Sciences. Part **b** reprinted with permission from ref. 155, American Chemical Society. Part **c** adapted from ref. 199, CC BY 3.0. Part **d** adapted with permission from ref. 267, American Chemical Society. Part **e** adapted with permission from ref. 271, American Chemical Society.

revealed that, in the as-deposited CoS_x catalyst, the cobalt atoms are surrounded by both sulfur and oxygen, whereas the cobalt centres are predominantly surrounded by a first shell of sulfur atoms during hydrogen evolution reaction catalytic activity[161]. The development of innovative water splitting technologies has also benefited from XAS investigations. For instance, the structure and oxidation state of ruthenium complexes that act as water oxidation catalysts was derived by XAS[162,163]. Another example is the use of XAS to identify the structure of highly active iron sites in an (Ni,Fe)OOH material for electrocatalytic water splitting[164]. Operando XAS and X-ray diffraction methods with subsecond time resolution revealed the ensemble of coexisting copper species on Cu_2O nanocube catalysts for CO_2 electroreduction with optimized potential pulses[165]. Perovskite-type oxide electrocatalysts have been studied extensively by XAFS[166]. $Ba_{0.5}Sr_{0.5}Co_{0.8}Fe_{0.2}O_3$, a benchmark electrocatalyst towards the oxygen evolution reaction, was investigated by operando XAS to determine that the in situ formed oxy(hydroxide) active layer is the real active species[167]. In addition, cobalt-based perovskites are known to possess elevated oxygen evolution reaction activity, which may be further enhanced by substituting cobalt with iron[168,169]. A recent investigation used operando EXAFS to study the $Ba_{0.5}Sr_{0.5}Co_{1-x}Fe_xO_{3-\delta}$ and $La_{0.2}Sr_{0.8}Co_{1-x}Fe_xO_{3-\delta}$ ($x = 0$ and 0.2) perovskites[170]. In these materials, XAS showed oxy(hydroxyde) layer formation without any changes in the local iron environment, improving the perovskite stability.

Extreme conditions and challenging samples

Probing the atomic structure and electronic properties of matter at extreme temperatures and pressures is another important XAFS application[171]. The combination of dedicated laser heating systems[172,173] together with XAS or crystallographic techniques has enabled melting curves to be determined for transition metal elements such as iron, cobalt and nickel up to the megabar range[174–176], together with the local structure of the compressed melts along the melting curve[177,178]. These results are relevant to geophysics and planetary sciences, where understanding the properties of metallic melts enables the behaviour of complex planetary bodies to be modelled, including the Earth. Energy dispersive XAS at the iron *K*-edge with a laser heating diamond anvil cell derived the melting temperature of iron at the core–mantle Earth boundary, equal to 4,250(±250) K at ~136 GPa (ref. 179).

XAS has important applications in the study of liquid systems that are challenging to investigate with other experimental techniques. The coordination properties of transition metal[180,181] and lanthanide and actinide[182,183] cations and halide anions[136,184–186] in water and organic solvents were studied by combining XAS and molecular dynamics simulations. High-quality structural models of the first coordination shell around the absorbing atom from theoretical simulations allow reliable analysis of the EXAFS data. From this, solvation geometries can be determined with unprecedented accuracy[137]. This combined approach also provided the first accurate determination of the ionic radii of lanthanide and actinide ions in aqueous solution[187,188].

Biological sciences

XAFS, both in the XANES and EXAFS regions, can investigate samples of biological interest, such as proteins and other macromolecules, cells and biological tissues. Metalloproteins have been investigated by XAS since first-generation synchrotrons[189]. Proteins containing metal ions are abundant, representing over one-third of all known expressed proteins[190]. The local structural and electronic properties around these metal centres may be studied by XAS of solution samples, which are close to in vivo conditions[191]. XANES studies have been performed on zinc metalloproteins[192] and neuroglobin[193]. Insights from EXAFS were combined with crystallographic information to investigate the copper site of azurin[194]. The cause of Alzheimer disease was investigated through solution redox chemistry on amyloid-β fragments with advanced XAS analysis[195–197]. HERFD EXAFS obtained accurate interatomic Fe–Fe distances for the *Q*-intermediate of methane monooxygenase[198] and information on the copper-active sites in particulate methane monooxygenase[199]. Another important application of XAS is the speciation of inorganic pharmaceutically active compounds before and after injection in the human body. XAS investigated how metal-based anticancer drugs operate, for instance, by demonstrating that carboplatin and oxaloplatin, two platin-based anticancer agents, are converted into cisplatin in solution. Oxaloplatin is a Pt(II) coordination compound widely used in cancer treatment[200]. Numerous other anticancer agents, such as arsenic, gold, selenium, gallium and cobalt compounds, have been studied by XAS[201–203]. Finally, the subchondral bones of human osteoarthritic knees were structurally investigated by phosphorous *K*-edge XAS[204].

Table 1 | Selected X-ray absorption spectroscopy applications

Discipline	Coupled technique	System	Ref.
Catalysis	Mössbauer, NRVS	Fe-zeolite	140
	–	Cu-zeolite	149
	–	High-entropy oxide	143
	DRIFTS	Ir single-atom catalyst	142
	EPR, GIWAXS	Ru complex	162
	UV–Vis	Fe complex	155
	Raman	CoS	161
	–	Perovskite oxide	167
Energy storage	–	High-entropy oxide	262
	–	Niobium oxide	263
	XRD, MD	Transition metal carbides	264
	TOF-SIMS	Solid–electrolyte interface	265
	XPS	Lithium thiophosphates	266
	XRD	Selenium sulfide	267
Extreme conditions	XRD	Ni metal	175
	–	Liquid Ni, Co	178
	XRD, SEM	Fe metal	179
	XMCD	3*d* metals	268
Solution chemistry	–	Co^{2+}, Ni^{2+}, Zn^{2+} solutions	180
	XRD	Lanthanide solutions	182
	–	Actinide solutions	188
	–	Br^- solutions	184
	NMR	Zn complexes	160
Molecular biology	–	Rubredoxin	189
	–	Zn metalloproteins	192
	MD	Neuroglobin	193
	XRD	Azurin	194
	–	Iron-tyrosinate proteins	269
Bio-medicine	–	As complexes	201
	–	Gold adducts of serum protein	202
	XRF	Selenite in lung cancer cells	203
	–	Alzheimer disease	196
	–	Platinum anticancer agents	200
	–	Subchondral bone	204
Environmental science	XRF	Exhaust particulates	270
	–	Incineration fly ash	219
	NMR	Soil	271
	NMR	Agro-industrial by-products	218
Geology	–	Biogenic magnetite	205
	Mössbauer	Green rust mineral	206
	XRD, FTIR	Soil clays	210
	–	Silicate glasses	211
Fundamental science	–	Advances in XAS and XES	67
Organometallics	–	Ferrocene conformation	114
Compounds	–	Nanostructure of compounds	223
Physics	–	New physical processes	225
Fluorescence	–	New structures in fluorescence	36
EELS	–	Low-energy electron scattering	224

DRIFTS, diffuse reflectance infrared Fourier transform spectroscopy; EELS, electron energy loss spectroscopy; EPR, electron paramagnetic resonance; FTIR, Fourier transform infrared; GIWAXS, grazing incidence wide angle X-ray scattering; MD, molecular dynamics; NRVS, nuclear resonance vibrational spectroscopy; SEM, scanning electron microscopy; TOF-SIMS: time-of-flight secondary ion mass spectrometry; XAS, X-ray absorption spectroscopy; XES, X-ray emission spectroscopy; XMCD, X-ray magnetic circular dichroism; XPS, X-ray photoelectron spectroscopy; XRD, X-ray diffraction; XRF, X-ray fluorescence.

Geology and environmental science

As XAFS measurements are essentially independent from the sample crystallinity, it is particularly successful in geochemistry, where highly disordered or amorphous systems are ubiquitous[205,206]. In situ XAS experiments have, for instance, enabled analysis of the computationally predicted hydrothermal geochemistry of Eu(II)/Eu(III), revealing that Eu(II) is increasingly stable at elevated temperatures but weakly coordinated by chloride ions[207]. Similar studies were also performed on aqueous nickel and cobalt chloride solutions, unveiling their speciation in hydrothermal fluids[208,209]. Solid systems of geochemical relevance, such as soil clays or silicate glasses, have also been analysed by XAFS[210,211]. Combined with X-ray diffraction, XAS determined the geochemical speciation of manganese in contaminated agricultural soils near historical mine tailings[212]. XAS spectra of mineral standards are important to interpret real-world samples. Systematic collections of mineral standards are often reported and available for the XAS community[213,214].

Disciplines closely related to geochemistry also routinely use XAS such as environmental science[215–218]. The composition of municipal fly ash[219], atmospheric aerosols[217], dust, particulate matter[215,220,221] and marine sediments has been explored by XAFS[221]. Lunar glass beads were analysed by in situ XAS experiments to determine the total Fe(III) content[222].

Fundamental physics and theory

Importantly, XAS studies continue to make breakthrough in fundamental science, whether concerning the theory and analysis of XAS and XES[36,67]; the relativistic quantum mechanics of molecular binding in organometallic chemistry; the conformation of ferrocene[114]; the basic understanding of reference atoms, metals and compounds[223]; or the inelastic mean free path of the photoelectron, for XAS, electron energy loss spectroscopy and low energy electron diffraction[224]. Such fundamental studies are discovering new physical processes using advanced techniques in XAS and XES[225]. Furthermore, the recent technique of XR-HERFD – developed from HERFD and RIXS but investigates 2D XAS and XES maps in new, extended-range regions – is able to discover new physical processes with XAS and XES. These new physical processes affect the interpretation of normal XAS data and theory on all materials.

Time-resolved experiments down to the millisecond timescale can also be carried out using the quick-EXAFS technique[226,227]. As synchrotron

technology improves, quick-EXAFS will become even more accessible, allowing a broader range of scientists to explore diverse systems, from biomaterials to advanced batteries. Future applications could also include observing the exact mechanisms of complex biological systems or tracking the evolution of nanoparticles in a reaction.

Reproducibility and data deposition

Reproducibility and statistical metrics have been discussed in XAS and separately for EXAFS and XANES for decades[228–232]. Some groups have been reporting uncertainties, error analysis and reproducibility for over 20 years[233,234]. Currently, these are considered non-standard techniques and relate to advanced methods, including XERT[64,235] and hybrid techniques[65,236]. A summary of data formats, metrics and how they have changed over time is given in ref. 237. Key issues are raised in refs. 129,238,239 and presented in ref. 68.

The standard XAS data set has no estimate of reproducibility, repeatability or precision. However, it is easy to repeat an identical scan or the count at each energy or k-value. This can be repeated, for example, up to 10 times to provide a good estimate of repeatability or precision at those experimental conditions. Without an investigation of systematics, these data may not be suitable for reporting or deposition. However, it is also easy to measure repeatedly, across the energy range, the dark current, blank current and dead time of the detector as appropriate. This can provide a beam-independent measurement, bringing the data to a quality suitable for deposition, which may be beamline-independent and cross-platform portable[69].

Ideally, counting statistics will be normally distributed. After the measurement, consistency from residual noise in E-space or χ versus k-space can be estimated. This usually requires an initial removal of errors and artefacts, such as Bragg diffraction glitches. There is also a de facto standard for estimating uncertainty from fast Fourier transformations into r-space, which is not mathematically or statistically justified. This often uses a transform of $k^2\chi$, which intrinsically distorts the data before the transform. These r-space approaches require a uniform experimental grid of data in k-space that is often not possible nor available. As a result, this type of method typically interpolates a non-uniform grid and estimates a single uncertainty in transformed space when the uncertainties of data points are individual. Typical FT artefacts from crystallography are not usually treated.

If these approaches succeed in assessing precision and repeatability, a careful error analysis should also consider systematics in transmission and fluorescence measurements. The aperture and bandwidth of the beam on the sample; the structure and heterogeneity of the sample; the monochromation and harmonics in the beam; and scattering effects all contribute[129,238,239]. A recent drive is to investigate these issues across different beamlines. The goal is to assess the beamline or laboratory independence of data and data portability, as required for data deposition[240]. This follows earlier studies[229,232,241–243].

Another widespread and common practice is for the beamline and synchrotron to retain all raw data for each experiment, subject to computing storage space. Raw data are excellent from a beamline scientist perspective to safely retain data; however, it is usually inappropriate for portable transfer, deposition and error analysis. Equally some data sets investigate reaction rates and redox or fast processes or are very extensive in array size, making storage required extremely large and presenting the data in a compact form is non-trivial.

Current perceptions on data deposition and reporting are that $[\mu/\rho]$ versus E is the most reliable and transferable file, with uncertainties and error analysis, and that common practices of μ versus E or $[\mu/\rho]^*_{pe}$ versus E are useful. Problems arise from reporting the transformed χ versus k or $k^2\chi$ versus k; however, these are still highly useful for subsequent analysis.

Limitations and optimizations

In many cases, XAS is the ideal technique to investigate dynamic process, especially where there is disorder, long-range disorder, local order, glasses, solutions or reactions. However, this is just a drop in the ocean, more details can be found in ref. 139, reviews and overviews, including textbooks. In some cases, beamline or laboratory optics are limited by beam flux, collimation, monochromation, harmonics, scattering and divergence, but often these can be independently measured and corrected to yield greater physical insight, often by two orders of magnitude or more.

Many users find limitations in the heterogeneity of their samples, or from radiation damage causing photoreduction or decomposition, especially for fragile and biomedical samples. These are real limitations; however, many fragile samples can be measured far beyond the XANES region and many heterogeneous samples can be mapped by X-ray fluorescence microprobe techniques. Better preparation can give more suitable samples, or the sample can be mapped across the cross-section in XAS or XERT. Errors in sample preparation, roughness, homogeneity, E_0, S_0^2 and scale can lead to errors in coordination number and other correlated parameters, including bond length. There are limitations related to the sample concentration required to obtain specific nanostructure or other information, and choice of technique: absorption, fluorescence, electron yield or other measurement mode[46].

Two rough standards of expectation should be understood, based on the measurement technique. For conventional XAS and XAFS, common beamline advice suggests that it is possible to determine nearest neighbour and other bonding radii to 0.02 Å. This will increase or decrease according to the data statistics, quality, systematic effects and beam optics. For example, an error in the edge energy determination of 10 eV in the definition of $k = 0$ or in the offset fitting parameter E_0 results in bond length errors of the order of 0.02 Å. Similarly, it is possible to directly determine the coordination number of a system to ±20–25% and the nearest neighbour scattering atom within one atomic number below $Z \simeq 17$ or within three atomic numbers between $20 < Z < 35$.

Conversely, with advanced techniques, for example, XERT[63,64,235] and hybrid techniques[65,66,236], the bonding of nearest neighbours can be determined to 0.1% or 0.002 Å. These techniques can measure absorption coefficients accurately to 0.01% or better; lattice spacing of crystalline solids to 0.1% or 0.002 Å; and coordination to better than 1%. Additionally, structures can be distinguished with no difference in coordination. This can be used, for example, to determine the confirmation of ferrocene or complex and fragile biomolecules, such as amyloid-β fragments in Alzheimer disease. These examples cover ideal metals and solids, in addition to binary compounds and solutions. In some cases, heterogeneity can preclude this level of accuracy. However, uniform, homogeneous pellets and homogeneous solutions can overcome these issues.

Conventional EXAFS can determine six to seven independent parameters from the data set, including E_0, different shell radii, thermal and static broadening parameters and other parameters including multipole analysis. Advanced techniques permit more detailed investigations of hypothetical structures or reaction intermediates, inelastic mean free paths and other questions. At its simplest, XAFS can confirm a structure, bonding or reaction intermediate. At best, it can independently determine new structures and hypotheses of nanostructures.

Glossary

χ
It is either the photoabsorption coefficient for an isolated atom with no electron interference or a semi-empirical spline or other background subtraction to approximate what this might be; or an estimated edge-jump amplitude.

Extended XAFS
(EXAFS). Refers to the region of the absorption spectrum from about 30 eV above the absorbing edge, which shows complex oscillations that explain the local order of any material, bonding and radial distances.

Fluorescence detection mode
The intensity of a particular fluorescence line emitted by the sample is measured as a function of energy. The ratio of the intensity of the fluorescence line and the intensity of the incident radiation is proportional to the absorption coefficient.

High-energy resolution fluorescence detection
The intensity of the emitted line of interest is recorded with a very narrow bandwidth as a function of the incident energy. The ratio to the incident intensity results in an X-ray absorption spectroscopy spectrum with sharper spectral features. Usually, this 1D spectrum is taken along the peak of the $K\alpha_1$ or $K\beta_{1,3}$ ridge to optimize flux and statistics.

k
k-space represents the spectrum in terms of the effective photoelectron wavenumber above the absorption edge E_0 rather than versus energy.

Photoelectron
An electron emitted into the continuum from a bound state in the atom or material when the incident energy of the photon is above the energy of the absorption edge.

Self-absorption
Also called over-absorption. The incident photon (X-ray) field is absorbed in the material and when it emits a fluorescent photon on relaxation, the fluorescent photon is absorbed as it passes through the material to the surface.

Transmission detection mode
The absorption spectrum is obtained by taking the natural logarithm of the ratio of the intensity of the radiation before and after the sample as a function of the incident energy. The measurement obtained is equal to the absorption coefficient.

X-ray absorption fine structure
(XAFS). The modulation of the absorption coefficient at and above an absorption edge of an element owing to its chemical state and the structure of its immediate surroundings. XAFS is commonly divided into the near-edge region (X-ray absorption near-edge structure or near-edge X-ray absorption fine structure), which extends to ~30 eV above the absorption edge, and the extended region that displays oscillations in the absorption coefficient extending from 30 eV above the absorption edge.

X-ray absorption near-edge structure
(XANES); also called NEXAFS (near-edge X-ray absorption fine structure). The region of the absorption spectrum that extends from below the edge to about 30 eV above the edge. It gives insight into local coordination, molecular bonding, oxidation state, geometry and Fermi level. Sometimes referred to as the X-ray absorption main edge structure region.

X-ray absorption spectroscopy
For a solid, liquid or disordered material, the measurement of the X-ray linear absorption coefficient $\mu_{pe}(E)$ or the mass absorption coefficient as a function of incident energy E.

X-ray emission spectroscopy
The measurement of the X-ray emission from a sample irradiated by X-rays.

X-ray mass absorption coefficient
Follows the Beer–Lambert law for a beam of photons of energy E in which the transmitted photon intensity $I(t)$ is related to the incoming photon intensity I_0.

Outlook

XAS is an established experimental technique for studying the electronic and local atomic structure of materials[40,42,137]. It has applications in many different disciplines, from physics, chemistry and catalysis to environmental science, materials science, biology and cultural heritage. There have been many notable advances in XAFS methodology and facilities, which are expected to continue to develop. These advances include improved sources with higher brilliance, coherence, microfocus and laboratory sources; time-resolved methods; new detectors, such as silicon drift detectors and pixel arrays; diffractive analysers, for instance, LERIX, HERIX and BCLA; improved open-source data analysis software, with automated methods incorporating improved theory, machine learning and neural nets; and extensions of XAFS to hybrid adjacent techniques, such as X-ray magnetic circular dichroism, diffraction anomalous fine structure, X-ray Raman and inelastic X-ray scattering[43].

Using high-brilliance third-generation and fourth-generation sources, XAS has investigated fast processes under operando conditions[244–246]. Combining techniques has been essential, as the increased complexity of problems requires multidisciplinary methods. Numerous examples can be found in the literature, in which combinations of techniques – such as XAS/DRIFTS/MS/UV–Vis, XAS/XRD/UV–Vis/Raman or SAXS/WAXS/Raman/UV–Vis – give a powerful approach to elucidate reaction mechanisms under operando conditions[247–251]. It is expected that in the next decade this area will become even more important. The enhanced brilliance of newly developed fourth-generation sources will enable faster processes to be studied. In addition, the smaller beam sizes of new sources will ease the design of complex sample environments needed to combine techniques. This could make it possible to add new tools, such as NMR spectroscopy or X-ray photoelectron spectroscopy.

Another area of expansion is to exploit photon-in/photon-out core-level spectroscopies[41,252,253]. Although outside the scope of this Primer, HERFD XAS, non-resonant XES, resonant XES and X-ray Raman

scattering are becoming increasingly relevant for the structural characterization of materials. Future developments of new instrumentation — detectors and optics — together with the new brilliant sources will enable these photon-hungry techniques to be applied to samples under more realistic operating conditions.

There will be a greater understanding of XAS theory and modelling in the coming years, including applications to RIXS, HERFD and XFELs. The development of new instrumentation and techniques will need to be supported by novel theoretical approaches[11,15,98,111,117,223,224,254–257] and advanced analysis methods[35,64,65,70]. Widespread definition, measurement and use of uncertainty in XAS, XES and related techniques will be welcomed, alongside packages to fit data with defined uncertainty for improved analysis accuracy[63,66,129]. An exciting future direction is ab initio and hypothesis testing of nanostructures with goodness-of-fit metrics. These developments will lead to robust, transferable experimental data sets and reference data.

When performing operando experiments, approaches based on machine learning may have an important role. This could enable on-the-fly results to direct experimental conditions, such as temperature, gas feedthrough concentration or data collection strategy. In addition, the increasing amount of data collected during the experiments may need automated approaches to select data with interesting results. Using deep neural networks to simulate spectroscopy experiments has shown promise[258,259]. Laboratory-based XAS/XES systems[260] will likely have a large impact in developing the technique, have an important role in collecting standard measurements and for training. There are also new and exciting techniques that were not able to be covered in this Primer[261].

Published online: 05 December 2024

References

1. Chantler, C. T. & Creagh, D. C. in *International Tables for Crystallography* Vol. I, Ch. 2.1 (eds Chantler, C. T., Bunker, B. A. & Boscherini, F.) 21–40 (Kluwer Academic Publishers, 2024).
   Encyclopaediac introduction to and summary of X-ray absorption spectroscopy and X-ray emission spectroscopy for users and experts.
2. Chantler, C. T. X in *International Tables for Crystallography* Vol. I, Ch. 9.1 (eds Chantler, C. T., Bunker, B. A. & Boscherini, F.) 1059–1067 (Kluwer Academic Publishers, 2024).
3. Ascone, I. & Chantler, C. T. XAFS-related entries in the online dictionary of crystallography. *IUCr* https://www.iucr.org/resources/commissions/xafs/xafs-related-definitions-for-the-iucr-dictionary (2021).
4. Chantler, C. T. & IUCr Commission on XAFS. in *A Little Dictionary of Crystallography* [*IUCR Commission on Crystallographic Nomenclature*] (eds Authier, A. & Chapuis, G.) 1–286 (Kluwer Academic Publishers, 2019).
5. Chantler, C. T. Theoretical form factor, attenuation, and scattering tabulation for *Z*=1–92 from *E*=1–10 eV to *E*=0.4–1.0 MeV. *J. Phys. Chem. Ref. Data* **24**, 71–643 (1995).
6. Chantler, C. T. et al. X-ray form factor, attenuation and scattering tables (version 2.0). *NIST* https://physics.nist.gov/PhysRefData/FFast/html/form.html (2000).
7. Chantler, C. T., Smale, L. F. & Hudson, L. T. in *International Tables for Crystallography* 4th edn, Vol. C, Ch. 4.2.2 (ed. Welberry, T. R.) (Wiley, in the press).
   Encyclopaedic explanation of matter–photon, electron–matter and neutron–matter interaction for crystallographers, diffraction, X-ray absorption spectroscopy and X-ray emission spectroscopy researchers.
8. Creagh, D. C. & Chantler, C. T. in *International Tables for Crystallography* 4th edn, Vol. C, Ch. 4.2.3 (ed. Welberry, T. R.) (Wiley, in the press).
9. Creagh, D. C. & Chantler, C. T. in *International Tables for Crystallography* 4th edn, Vol. C, Ch. 4.2.4 (ed. Welberry, T. R.) (Wiley, in the press).
10. Kraft, S., Stümpel, J., Becker, P. & Kuetgens, U. High resolution X-ray absorption spectroscopy with absolute energy calibration for the determination of absorption edge energies. *Rev. Sci. Instrum.* **67**, 681–687 (1996).
11. Chantler, C. T. & Bourke, J. D. in *International Tables for Crystallography* Vol. I, Ch. 2.25 (eds Chantler, C. T., Bunker, B. A. & Boscherini, F.) 230–269 (Kluwer Academic Publishers, 2024).
12. Durham, P. J. in *EXAFS and Near Edge Structure* (eds Bianconi, A., Incoccia, L. & Stipcich, S.) 37–43 (Springer, 1983).
    Overview, both introductory and more detailed, of synchrotron techniques and applications.
13. Durham, P. J. in *X-ray Absorption: Principles, Applications, Techniques of EXAFS, SEXAFS and XANES* (eds Koningsberger, D. C. & Prins, R.) 53–84 (Wiley, 1988).
14. Natoli, C. R., Hatada, K. & Sebilleau, D. in *International Tables for Crystallography* Vol. I, Ch. 2.3 (eds Chantler, C. T., Bunker, B. A. & Boscherini, F.) 48–54 (Kluwer Academic Publishers, 2024).
15. Kas, J. J., Rehr, J. J. & Vila, F. D. in *International Tables for Crystallography* Vol. I, Ch. 2.10 (eds Chantler, C. T., Bunker, B. A. & Boscherini, F.) 107–113 (Kluwer Academic Publishers, 2024).
16. Crasemann, B. in *Atomic, Molecular and Optical Physics Handbook* (ed. Drake, G. W. F.) 701–711 (AIP, 1996).
17. Kissell, L. & Pratt, R. H. in *Atomic Inner-Shell Physics* (ed. Crasemann, B.) 465–711 (AIP, 1985).
18. Kane, P. P., Kissell, L., Pratt, R. P. & Roy, S. C. Elastic scattering of gamma rays and X-rays by atoms. *Phys. Rep.* **140**, 75–159 (1986).
19. Strutt, J. W. On the light from the sky, its polarization and colour. *Phil. Mag.* **41**, 107–120 (1871).
20. Strutt, J. W. On the scattering of light by small particles. *Phil. Mag.* **41**, 447–447 (1871).
21. Thomson, J. J. *Conduction of Electricity Through Gases* 2nd edn (Cambridge Univ. Press, 1906).
22. Delbruck, M. Note added in proof to L. Meitner and H. Kosters. *Z. Phys.* **84**, 137 (1933).
23. Papatzacos, P. & Mork, K. Delbruck scattering calculations. *Phys. Rev. D* **12**, 206 (1975).
24. Milstein, A. I. & Schumacher, M. Present status of Delbruck scattering. *Phys. Rep.* **243**, 183–214 (1994).
25. Compton, A. H. The total reflexion of X-rays. *Phil. Mag.* **45**, 1121 (1923).
26. Compton, A. H. The spectrum of scattered X-rays. *Phys. Rev.* **22**, 409 (1923).
27. Lee, P. A. & Pendry, J. B. Theory of the extended X-ray absorption fine structure. *Phys. Rev. B* **11**, 2795–2811 (1975).
28. Gurman, S. J., Binstead, N. & Ross, I. A rapid, exact, curved-wave theory for EXAFS calculations: II The multiple-scattering contributions. *J. Phys. C* **19**, 1845–1861 (1986).
29. Bunker, G. Application of the ratio method of EXAFS analysis to disordered systems. *Nucl. Instrum. Methods Phys. Res.* **207**, 437–444 (1983).
30. Fornasini, P. in *International Tables for Crystallography* Vol. I, Ch. 2.14 (eds Chantler, C. T., Bunker, B. A. & Boscherini, F.) 139–146 (Kluwer Academic Publishers, 2024).
31. Lee, P. A., Citrin, P. H., Eisenberger, P. & Kincaid, B. M. Extended X-ray absorption fine structure — its strengths and limitations as a structural tool. *Rev. Modern Phys.* **53**, 769–806 (1981).
    One of the first major overviews of extended X-ray absorption fine structure analysis and value.
32. Stern, E. A. in *X-ray Absorption: Principles, Applications, Techniques of EXAFS, SEXAFS and XANES* (eds Koningsberger, D. C. & Prins, R.) 3–51 (Wiley, 1988).
33. Jaklevic, J. et al. Fluorescence detection of EXAFS: sensitivity enhancement for dilute species and thin films. *Solid State Commun.* **23**, 679–682 (1977).
34. Chantler, C. T. et al. Stereochemical analysis of ferrocene and the uncertainty of fluorescence XAFS data. *J. Synchrotron Radiat.* **19**, 145–158 (2012).
35. Trevorah, R. M., Chantler, C. T. & Schalken, M. J. Solving self-absorption in fluorescence. *IUCrJ* **6**, 586–602 (2019).
36. Trevorah, R. M., Chantler, C. T. & Schalken, M. J. New features observed in self-absorption-corrected X-ray fluorescence spectra for Ni complexes with uncertainties. *J. Phys. Chem. A* **124**, 1634–1647 (2020).
37. Troger, L., Arvanitis, D. & Baberschke, K. Full correction of the absorption in soft-fluorescence extended X-ray absorption fine structure. *Phys. Rev. B* **46**, 3283–3289 (1992).
38. Pfalzer, P. et al. Elimination of self-absorption in fluorescence hard-X-ray absorption spectra. *Phys. Rev. B* **60**, 9335–9339 (1999).
39. Booth, C. H. & Bridges, F. Improved self-absorption correction for fluorescence measurements of extended X-ray absorption fine-structure. *Phys. Scr.* **T115**, 202–204 (2005).
40. Bunker, G. *Introduction to XAFS: A Practical Guide to X-ray Absorption Fine Structure Spectroscopy* (Cambridge Univ. Press, 2010).
    Excellent introduction to X-ray absorption spectroscopy theory, experiment and analysis.
41. van Bokhoven, J. & Lamberti, A. C. *X-Ray Absorption and X-Ray Emission Spectroscopy: Theory and Applications* (Willey, 2017).
42. Evans, J. *Absorption Spectroscopy for the Chemical and Materials Sciences* (Willey, 2017).
43. Chantler, C. T., Bunker, B. A. & Boscherini, F. (eds) *International Tables for Crystallography* Vol. I (Kluwer Academic Publishers, 2024).
44. Glatzel, P., Juhin, A. & Moretti, M. in *International Tables for Crystallography* Vol. I, Ch. 2.19 (eds Chantler, C. T., Bunker, B. A. & Boscherini, F.) 177–189 (Kluwer Academic Publishers, 2024).
45. Glatzel, P. & Ghiringhelli, G. in *International Tables for Crystallography* Vol. I, Ch. 3.49 (eds Chantler, C. T., Bunker, B. A. & Boscherini, F.) 586–591 (Kluwer Academic Publishers, 2024).
46. Chantler, C. T. in *International Tables for Crystallography* Vol. I, Ch. 2.8 (eds Chantler, C. T., Bunker, B. A. & Boscherini, F.) 88–99 (Kluwer Academic Publishers, 2024).
47. d'Acapito, F. in *International Tables for Crystallography* Vol. I, Ch. 3.32 (eds Chantler, C. T., Bunker, B. A. & Boscherini, F.) 504–507 (Kluwer Academic Publishers, 2024).
48. d'Acapito, F. in *International Tables for Crystallography* Vol. I, Ch. 4.5 (eds Chantler, C. T., Bunker, B. A. & Boscherini, F.) 613–616 (Kluwer Academic Publishers, 2024).

49. Stern, E. A. Theory of the extended X-ray-absorption fine structure. *Phys. Rev. B* **10**, 3027–3037 (1974).
50. Lytle, F. W., Sayers, D. E. & Stern, E. A. Extended X-ray-absorption fine-structure technique. II. Experimental practice and selected results. *Phys. Rev. B* **11**, 4825–4835 (1975).
51. Stern, E. A., Sayers, D. E. & Lytle, F. W. Extended X-ray-absorption fine-structure technique. III. Determination of physical parameters. *Phys. Rev. B* **11**, 4836 (1975).
52. Stern, E. A. & Heald, S. M. in *Handbook of Synchrotron Radiation* Vol. 1b (ed. Koch, E. E.) (North Holland Publishing Company, 1983).
53. Koningsberger, D. C. & Prins, R. *X-ray Absorption: Principles, Applications, Techniques of EXAFS, SEXAFS and XANES* (John Wiley and Sons Inc., 1987).
Excellent overview of different X-ray absorption spectroscopy developments.
54. Boscherini, F. in *International Tables for Crystallography* Vol. I, Ch. 1.2 (eds Chantler, C. T., Bunker, B. A. & Boscherini, F.) 10–12 (Kluwer Academic Publishers, 2024).
55. Einfeld, D., Plesko, M. & Schaper, J. First multi-bend achromat lattice consideration. *J. Synchrotron Radiat.* **21**, 856–861 (2014).
56. Shin, S. New era of synchrotron radiation: fourth-generation storage ring. *AAPPS Bull.* **31**, 1–16 (2021).
57. Diaz-Moreno, S. in *International Tables for Crystallography* Vol. I, Ch. 3.48 (eds Chantler, C. T., Bunker, B. A. & Boscherini, F.) 581–585 (Kluwer Academic Publishers, 2024).
58. Bès, R. et al. Laboratory-scale X-ray absorption spectroscopy approach for actinide research: experiment at the uranium *L*3-edge. *J. Nucl. Mater.* **507**, 50–53 (2018).
59. Geloni, G. et al. Coherence properties of the European XFEL. *N. J. Phys.* **12**, 035021 (2010).
60. Pandey, S. et al. Time-resolved serial femtosecond crystallography at the European XFEL. *Nat. Methods* **3**, 73–78 (2020).
61. Lindroth, E. et al. Challenges and opportunities in attosecond and XFEL science. *Nat. Rev. Phys.* **1**, 107–111 (2019).
62. Cauchois, Y. Spectrographie des rayons X par transmission d'un faisceau non canalisé à travers un cristal courbé-i. *J. Phys. Rad.* **3**, 320–336 (1932).
63. Ekanayake, R. S. K. et al. High-accuracy mass attenuation coefficients and X-ray absorption spectroscopy of zinc — the first X-ray extended range technique-like experiment in Australia. *J. Synchrotron Radiat.* **28**, 1476–1491 (2021).
64. Chantler, C. T. in *International Tables for Crystallography* Vol. I, Ch. 3.43 (eds Chantler, C. T., Bunker, B. A. & Boscherini, F.) 558–563 (Kluwer Academic Publishers, 2024).
65. Best, S. P. & Chantler, C. T. in *International Tables for Crystallography* Vol. I, Ch. 3.14 (eds Chantler, C. T., Bunker, B. A. & Boscherini, F.) 375–394 (Kluwer Academic Publishers, 2024).
66. John, M. W. et al. High accuracy transmission and fluorescence XAFS of zinc at 10 K, 50 K, 100 K and 150 K using the Hybrid technique. *J. Synchrotron Radiat.* **30**, 147–168 (2023).
67. Schalken, M. J. & Chantler, C. T. Propagation of uncertainty in experiment: structures of Ni (II) coordination complexes. *J. Synchrotron Radiat.* **25**, 920–934 (2018).
68. Chantler, C. T. in *International Tables for Crystallography* Vol. I, Ch. 4.6 (eds Chantler, C. T., Bunker, B. A. & Boscherini, F.) 617–623 (Kluwer Academic Publishers, 2024).
69. Chantler, C. T. in *International Tables for Crystallography* Vol. I, Ch. 4.7 (eds Chantler, C. T., Bunker, B. A. & Boscherini, F.) 624–630 (Kluwer Academic Publishers, 2024).
70. Chantler, C. T. in *International Tables for Crystallography* Vol. I, Ch. 5.7 (eds Chantler, C. T., Bunker, B. A. & Boscherini, F.) 664–671 (Kluwer Academic Publishers, 2024).
71. Bunker, G. in *International Tables for Crystallography* Vol. I, Ch. 3.12 (eds Chantler, C. T., Bunker, B. A. & Boscherini, F.) 365–369 (Kluwer Academic Publishers, 2024).
72. Parratt, L. G., Hempstead, C. F. & Jossem, E. L. 'Thickness effect' in absorption spectra near absorption edges. *Phys. Rev.* **105**, 1228–1232 (1957).
73. Stern, E. A. & Kim, K. Thickness effect on the extended-X-ray-absorption-fine-structure amplitude. *Phys. Rev. B* **23**, 3781–3787 (1981).
74. Bridges, F. in *International Tables for Crystallography* Vol. I, Ch. 3.13 (eds Chantler, C. T., Bunker, B. A. & Boscherini, F.) 370–374 (Kluwer Academic Publishers, 2024).
75. Bridges, F. & Booth, C. H. in *International Tables for Crystallography* Vol. I, Ch. 3.44 (eds Chantler, C. T., Bunker, B. A. & Boscherini, F.) 564–566 (Kluwer Academic Publishers, 2024).
76. Achkar, A. et al. Bulk sensitive X-ray absorption spectroscopy free of self-absorption effects. *Phys. Rev. B* **83**, 081106 (2011).
77. Bunker, G. B. *A X-Ray Absorption Study of Transition Metal Oxides*. PhD thesis (1984).
78. Zhang, K., Rosenbaum, G. & Bunker, G. The correction of the dead time loss of the Ge detector in X-ray absorption spectroscopy. *Jpn. J. Appl. Phys.* **32**, 147 (1993).
79. Fister, T. et al. Multielement spectrometer for efficient measurement of the momentum transfer dependence of inelastic X-ray scattering. *Rev. Sci. Instrum.* **77**, 063901 (2006).
80. Gog, T. et al. Momentum-resolved resonant and nonresonant inelastic X-ray scattering at the advanced photon source. *Synchrotron Radiat. News* **22**, 12–21 (2009).
81. Zhong, Z. et al. A bent Laue analyzer for fluorescence EXAFS detection. *J. Synchrotron Radiat.* **6**, 212–214 (1999).
82. Natoli, C. R. in *EXAFS and Near Edge Structure* (eds Bianconi, A., Inoccia, L. & Stipcich, S.) 43–56 (Springer-Verlag, 1983).
83. Shadle, E. et al. X-ray absorption spectroscopic studies of the blue copper site: metal and ligand K-edge studies to probe the origin of the EPR hyperfine splitting in plastocyanin. *J. Am. Chem. Soc.* **115**, 767–776 (1993).
84. Dubois, J. L. et al. A systematic K-edge X-ray absorption spectroscopic study of Cu(III) sites. *J. Am. Chem. Soc.* **122**, 5775–5787 (2000).
85. George, S. D. et al. Spectroscopic investigation of stellacyanin mutants: axial ligand interactions at the blue copper site. *J. Am. Chem. Soc.* **125**, 11314–11328 (2003).
86. Baker, M. L. et al. K- and L-edge X-ray absorption spectroscopy (XAS) and resonant inelastic X-ray scattering (RIXS) determination of differential orbital covalency (DOC) of transition metal sites. *Coord. Chem. Rev.* **345**, 182–208 (2017).
87. Shulman, R. G., Yafet, Y., Eisenberger, P. & Blumberg, W. E. Observation and interpretation of X-ray absorption edges in iron compounds and proteins. *Proc. Natl Acad. Sci. USA* **73**, 1384–1388 (1976).
88. Hahn, J. E. et al. Observation of an electric quadrupole transition in the X-ray absorption spectrum of a Cu(II) complex. *Chem. Phys. Lett.* **88**, 595–598 (1982).
89. Sarangi, R. et al. X-ray absorption edge spectroscopy and computational studies on $LCuO_2$ species: superoxide-Cu^{II} versus peroxide-Cu^{III} bonding. *J. Am. Chem. Soc.* **128**, 8286–8296 (2006).
90. Yamamoto, T. in *International Tables for Crystallography* Vol. I, Ch. 2.7 (eds Chantler, C. T., Bunker, B. A. & Boscherini, F.) 80–87 (Kluwer Academic Publishers, 2024).
91. Press, W. H., Teukolsky, S. A., Vetterling, W. T. & Flannery, B. P. *Numerical Recipes: The Art of Scientific Computing* Vol. 1, 3rd edn (Cambridge Univ. Press, 2007).
92. Webb, S. M. in *International Tables for Crystallography* Vol. I, Ch. 5.17 (eds Chantler, C. T., Bunker, B. A. & Boscherini, F.) 709–715 (Kluwer Academic Publishers, 2024).
93. Wasserman, S. R. The analysis of mixtures: application of principal component analysis to XAS spectra. *J. Phys. IV* **7**, C2–C203 (1997).
94. Wasserman, S. R., Allen, P. G., Shuh, K., Bucher, J. J. & Edelstein, N. M. EXAFS and principal component analysis: a new shell game. *J. Synchrotron Radiat.* **6**, 284–286 (1999).
95. Tauler, R. Multivariate curve resolution applied to second order data. *Chemom. Intell. Lab. Syst.* **30**, 133–146 (1995).
96. de Juan, A. & Tauler, R. Multivariate curve resolution (MCR) from 2000: progress in concepts and applications. *Crit. Rev. Anal. Chem.* **36**, 163–176 (2007).
97. Conti, P., Zamponi, S., Giorgetti, M., Berrettoni, M. & Smyrl, W. H. Multivariate curve resolution analysis for interpretation of dynamic Cu *k*-edge X-ray absorption spectroscopy spectra for a Cu doped V_2O_5 lithium battery. *Anal. Chem.* **82**, 3629–3635 (2010).
98. Bourke, J. D., Chantler, C. T. & Joly, Y. FDMX: extended X-ray absorption fine structure calculations using the finite difference method. *J. Synchrotron Radiat.* **23**, 551–559 (2016).
Discussion of merging the X-ray absorption near-edge structure and extended X-ray absorption fine structure regions with a single theoretical model.
99. de Groot, F. in *International Tables for Crystallography* Vol. I, Ch. 2.4 (eds Chantler, C. T., Bunker, B. A. & Boscherini, F.) 55–59 (Kluwer Academic Publishers, 2024).
100. Haverkort, M. W., Zwierzycki, M. & Andersen, O. K. Multiplet ligand-field theory using Wannier orbitals. *Phys. Rev. B* **85**, 165113 (2012).
101. Bianconi, A. et al. Multielectron excitations in the K-edge X-ray-absorption near-edge spectra of V, Cr, and Mn 3d0 compounds with tetrahedral coordination. *Phys. Rev. B* **43**, 6885–6892 (1991).
102. Rehr, J. J. & Ankudinov, A. L. Progress in the theory and interpretation of XANES. *Coord. Chem. Rev.* **249**, 131–140 (2005).
103. Benfatto, M. & Della Longa, S. Geometrical fitting of experimental XANES spectra by a full multiple-scattering procedure. *J. Synchrotron Radiat.* **8**, 1087–1094 (2001).
104. Benfatto, M., Della Longa, S. & Natoli, C. R. The *M*XAN procedure: a new method for analysing the XANES spectra of metalloproteins to obtain structural quantitative information. *J. Synchrotron Radiat.* **10**, 51–57 (2003).
105. Joly, Y., Cabaret, D., Renevier, H. & Natoli, C. R. Electron population analysis by full-potential X-ray absorption simulations. *Phys. Rev. Lett.* **82**, 1–4 (1999).
106. Joly, Y. X-ray absorption near-edge structure calculations beyond the muffin-tin approximation. *Phys. Rev. B* **63**, 125120–125130 (2001).
107. Scandolo, S. et al. First-principles codes for computational crystallography in the Quantum-ESPRESSO package. *Z. Kristallog.* **220**, 574–579 (2005).
108. Kresse, G. & Hafner, J. Ab initio molecular dynamics for liquid metals. *Phys. Rev. B* **47**, 558–561 (1993).
109. Kresse, G. Ab initio molecular-dynamics simulation of the liquid–metal–amorphous–semiconductor transition in germanium. *Phys. Rev. B* **48**, 15 (1994).
110. Blaha, P. in *International Tables for Crystallography* Vol. I, Ch. 2.12 (eds Chantler, C. T., Bunker, B. A. & Boscherini, F.) 121–129 (Kluwer Academic Publishers, 2024).
111. Joly, Y., Ramos, A. Y. & Bunau, O. in *International Tables for Crystallography* Vol. I, Ch. 2.11 (eds Chantler, C. T., Bunker, B. A. & Boscherini, F.) 114–120 (Kluwer Academic Publishers, 2024).
112. Neese, F. The ORCA program system. *Wiley Interdiscip. Rev. Comput. Mol. Sci.* **2**, 73–78 (2012).
113. te Veide, G. et al. Chemistry with ADF. *J. Comput. Chem.* **22**, 931–967 (2001).
114. Bourke, J. D. et al. Conformation analysis of ferrocene and decamethylferrocene via full-potential modeling of XANES and XAFS spectra. *J. Phys. Chem. Lett.* **7**, 2792–2796 (2016).
115. Shirley, E. L. Ab initio inclusion of electron–hole attraction: application to X-ray absorption and resonant inelastic X-ray scattering. *Phys. Rev. Lett.* **80**, 794–797 (1998).
116. Vinson, J., Rehr, J. J., Kas, J. J. & Shirley, E. L. Bethe–Salpeter equation calculations of core excitation spectra. *Phys. Rev. B* **83**, 115106 (2011).
117. Shirley, E. L., Pettersson, L. G. M. & Prendergast, D. in *International Tables for Crystallography* Vol. I, Ch. 2.13 (eds Chantler, C. T., Bunker, B. A. & Boscherini, F.) 130–138 (Kluwer Academic Publishers, 2024).

118. Sagmeister, S. & Ambrosch-Draxl, C. Time-dependent density functional theory versus Bethe–Salpeter equation: an all-electron study. *Phys. Chem. Chem. Phys.* **11**, 4451–4457 (2009).
119. Elliott, J. D. et al. Web-CONEXS: an inroad to theoretical X-ray absorption spectroscopy. *J. Synchrotron Radiat.* **31**, 1276–1284 (2024).
120. Zabinsky, S. I., Rehr, J. J., Ankudinov, A., Albers, R. C. & Eller, M. J. Multiple-scattering calculations of X-ray-absorption spectra. *Phys. Rev. B* **52**, 2995–3009 (1995).
121. Filipponi, A. & Di Cicco, A. X-ray-absorption spectroscopy and *n*-body distribution functions in condensed matter. II. Data analysis and applications. *Phys. Rev. B* **52**, 15135–15149 (1995).
122. Binsted, N., Norman, D. & Gurman, S. J. A rapid, exact, curved-wave theory for EXAFS calculations. II. The multiple-scattering contributions. *J. Phys. C* **19**, 1845–1861 (1986).
123. Bourke, J. D. & Chantler, C. T. Finite difference method calculations of long-range X-ray absorption fine structure for copper over $k \simeq 20$ Å^{-1}. *Nucl. Instrum. Meth. A* **619**, 33–36 (2010).
124. Rehr, J. J., de Leon, J. M., Zabinsky, S. I. & Albers, R. C. Theoretical approaches to X-ray absorption fine-structure standards. *J. Am. Chem. Soc.* **113**, 5135–5140 (1991).
125. Koningsberger, D. C., Mojet, B. L., van Dorssen, G. E. & Ramaker, D. E. XAFS spectroscopy; fundamental principles and data analysis. *Top. Catal.* **10**, 143–155 (2000).
126. Cook, J. W. & Sayers, D. E. Criteria for automatic X-ray absorption fine structure background removal. *J. Appl. Phys.* **52**, 5024 (1998).
127. Ravel, B. & Newville, M. ATHENA, ARTEMIS, HEPHAESTUS: data analysis for X-ray absorption spectroscopy using IFEFFIT. *J. Synchrotron Radiat.* **12**, 537–541 (2005).
128. Chantler, C. T. in *International Tables for Crystallography* Vol. I, Ch. 5.6 (eds Chantler, C. T., Bunker, B. A. & Boscherini, F.) 659–663 (Kluwer Academic Publishers, 2024).
129. Chantler, C. T., Barnea, Z., Tran, C. Q. & Rae, N. A. A step toward standardization: development of accurate measurements of X-ray absorption and fluorescence. *J. Synchrotron Radiat.* **19**, 851–862 (2012).
130. Rehr, J. J., Stern, E. A., Martin, R. L. & Davidson, E. R. Extended X-ray-absorption fine-structure amplitudes — wave-function relaxation and chemical effects. *Phys. Rev. B* **17**, 560 (1978).
131. Newville, M. *Fundamentals of XAFS* (CARS, University of Chicago, 2004).
132. Michalowicz, A. & Vlaic, G. Multiple solutions in data fitting: a trap in EXAFS structural analysis and some ideas to avoid it. *J. Synchrotron Radiat.* **5**, 1317–1320 (1998).
133. Tran, C. Q., Chantler, C. T. & de Jonge, M. D. in *International Tables for Crystallography* Vol. I, Ch. 3.42 (eds Chantler, C. T., Bunker, B. A. & Boscherini, F.) 549–557 (Kluwer Academic Publishers, 2024).
134. Yevick, A. & Frenkel, A. I. Effects of surface disorder on EXAFS modeling of metallic clusters. *Phys. Rev. B* **81**, 115451 (2010).
135. Filipponi, A. & D'Angelo, P. *XAS in Liquid Systems* 745–771 (John Wiley & Sons, 2016).
136. D'Angelo, P., Di Nola, A., Filipponi, A., Pavel, N. V. & Roccatano, D. An extended X-ray absorption fine structure study of aqueous solutions by employing molecular dynamics simulations. *J. Chem. Phys.* **100**, 985 (1994).
137. Filipponi, A. EXAFS for liquids. *J. Phys. Condens. Matter* **13**, R23 (2001).
138. Timoshenko, J. & Frenkel, A. I. Probing structural relaxation in nanosized catalysts by combining EXAFS and reverse Monte Carlo methods. *Catal. Today* **280**, 274–282 (2017).
139. Chantler, C. T., Bunker, B. A. & Boscherini, F. (eds) in *International Tables for Crystallography* Vol. I, Part 8 (Kluwer Academic Publishers, 2024).
140. Snyder, B. E. R. et al. Structural characterization of a non-heme iron active site in zeolites that hydroxylates methane. *Proc. Natl Acad. Sci. USA* **115**, 4565–4570 (2018).
141. Pappas, D. K. et al. Methane to methanol: structure–activity relationships for Cu-CHA. *J. Am. Chem. Soc.* **139**, 14961–14975 (2017).
142. Lu, Y. et al. Identification of the active complex for CO oxidation over single-atom Ir-on-$MgAl_2O_4$ catalysts. *Nat. Catal.* **2**, 149–156 (2019).
143. Fracchia, M. et al. Stabilization by configurational entropy of the Cu(ii) active site during CO oxidation on $Mg_{0.2}Co_{0.2}Ni_{0.2}Cu_{0.2}Zn_{0.2}O$. *J. Phys. Chem. Lett.* **11**, 3589–3593 (2020).
144. Kulkarni, A. R., Zhao, Z.-J., Siahrostami, S., Nørskov, J. K. & Studt, F. Monocopper active site for partial methane oxidation in Cu-exchanged 8MR zeolites. *ACS Catal.* **6**, 6531–6536 (2016).
145. Alayon, E. M. C., Nachtegaal, M., Bodi, A. & van Bokhoven, J. A. Reaction conditions of methane-to-methanol conversion affect the structure of active copper sites. *ACS Catal.* **4**, 16–22 (2014).
146. Grundner, S. et al. Single-site trinuclear copper oxygen clusters in mordenite for selective conversion of methane to methanol. *Nat. Commun.* **6**, 7546 (2015).
147. Tomkins, P., Ranocchiari, M. & van Bokhoven, J. A. Direct conversion of methane to methanol under mild conditions over Cu-zeolites and beyond. *Acc. Chem. Res.* **50**, 418–425 (2017).
148. Narsimhan, K., Iyoki, K., Dinh, K. & Román-Leshkov, Y. Catalytic oxidation of methane into methanol over copper-exchanged zeolites with oxygen at low temperature. *ACS Cent. Sci.* **2**, 424–429 (2016).
149. Pappas, D. K. et al. The nuclearity of the active site for methane to methanol conversion in Cu-mordenite: a quantitative assessment. *J. Am. Chem. Soc.* **140**, 15270–15278 (2018).
150. Deka, U., Lezcano-Gonzalez, I., Weckhuysen, B. M. & Beale, A. M. Local environment and nature of Cu active sites in zeolite-based catalysts for the selective catalytic reduction of NO_x. *ACS Catal.* **3**, 413–427 (2013).
151. Beale, A. M., Gao, F., Lezcano-Gonzalez, I., Peden, C. H. F. & Szanyi, J. Recent advances in automotive catalysis for NO_x emission control by small-pore microporous materials. *Chem. Soc. Rev.* **44**, 7371–7405 (2015).
152. Paolucci, C. et al. Dynamic multinuclear sites formed by mobilized copper ions in NO_x selective catalytic reduction. *Science* **357**, 898–903 (2017).
153. Paolucci, C. et al. Catalysis in a cage: condition-dependent speciation and dynamics of exchanged Cu cations in SSZ-13 zeolites. *J. Am. Chem. Soc.* **138**, 6028–6048 (2016).
154. Lomachenko, K. A. et al. The Cu-CHA denox catalyst in action: temperature-dependent NH_3-assisted selective catalytic reduction monitored by operando XAS and XES. *J. Am. Chem. Soc.* **138**, 12025–12028 (2016).
155. Capocasa, G. et al. Coupled X-ray absorption/UV–Vis monitoring of fast oxidation reactions involving a nonheme iron-Oxo complex. *J. Am. Chem. Soc.* **141**, 2299–2304 (2019).
156. Tavani, F. et al. Direct mechanistic evidence for a non-heme complex reaction through a multivariate XAS analysis. *Inorg. Chem.* **59**, 9979–9989 (2020).
157. Tavani, F. et al. Direct structural and mechanistic insights into fast bimolecular chemical reactions in solution through a coupled XAS/UV–Vis multivariate statistical analysis. *Dalton Trans.* **50**, 131–142 (2021).
158. Tavani, F. et al. Activation of C–H bonds by a nonheme iron(iv)–oxo complex: mechanistic evidence through a coupled EDXAS/UV–Vis multivariate analysis. *Phys. Chem. Chem. Phys.* **23**, 1188–1196 (2021).
159. Del Giudice, D. et al. Two faces of the same coin: coupling X-ray absorption and NMR spectroscopies to investigate the exchange reaction between prototypical Cu coordination complexes. *Chem. Eur. J.* **28**, e202103825 (2022).
160. Frateloreto, F. et al. Following a silent metal ion: a combined X-ray absorption and nuclear magnetic resonance spectroscopic study of the Zn^{2+} cation dissipative translocation between two different ligands. *J. Phys. Chem. Lett.* **13**, 5522–5529 (2022).
161. Kornienko, N. et al. Operando spectroscopic analysis of an amorphous cobalt sulfide hydrogen evolution electrocatalyst. *J. Am. Chem. Soc.* **137**, 7448–7455 (2015).
162. Gil-Sepulcre, M. et al. Surface-promoted evolution of Ru-bda coordination oligomers boosts the efficiency of water oxidation molecular anodes. *J. Am. Chem. Soc.* **143**, 11651–11661 (2021).
163. Levin, N. et al. XAS and EPR in situ observation of Ru(v) oxo intermediate in a Ru water oxidation complex. *ChemElectroChem* **9**, e202101271 (2022).
164. Friebel, D. et al. Identification of highly active Fe sites in (Ni,Fe)OOH for electrocatalytic water splitting. *J. Am. Chem. Soc.* **137**, 1305–1313 (2015).
165. Timoshenko, J. et al. Steering the structure and selectivity of CO_2 electroreduction catalysts by potential pulses. *Nat. Catal.* **5**, 259–267 (2022).
166. Sun, H. & Zhou, W. Progress on X-ray absorption spectroscopy for the characterization of perovskite-type oxide electrocatalysts. *Energy Fuels* **35**, 5716–5737 (2021).
167. Suntivich, J., May, K. J., Gasteiger, H. A., Goodenough, J. B. & Shao-Horn, Y. A perovskite oxide optimized for oxygen evolution catalysis from molecular orbital principles. *Science* **334**, 1383–1385 (2011).
168. Zhang, S. et al. The latest development of CoOOH two-dimensional materials used as OER catalysts. *Chem. Commun.* **56**, 15387–15405 (2020).
169. Feng, C. et al. Fe-based electrocatalysts for oxygen evolution reaction: progress and perspectives. *ACS Catal.* **10**, 4019–4047 (2020).
170. Kim, B.-J. et al. Functional role of Fe-doping in Co-based perovskite oxide catalysts for oxygen evolution reaction. *J. Am. Chem. Soc.* **141**, 5231–5240 (2019).
171. Cerantola, V. et al. New frontiers in extreme conditions science at synchrotrons and free electron lasers. *J. Condens. Matter Phys.* **33**, 274003 (2021).
172. Aprilis, G. et al. Portable double-sided pulsed laser heating system for time-resolved geoscience and materials science applications. *Rev. Sci. Instrum.* **88**, 084501 (2017).
173. Kantor, I., Marini, C., Mathon, O. & Pascarelli, S. A laser heating facility for energy-dispersive X-ray absorption spectroscopy. *Rev. Sci. Instrum.* **89**, 013111 (2018).
174. Anzellini, S., Dewaele, A., Mezouar, M., Loubeyre, P. & Morard, G. Melting of iron at earth's inner core boundary based on fast X-ray diffraction. *Science* **340**, 464–466 (2013).
175. Boccato, S. et al. The melting curve of nickel up to 100 GPa explored by XAS. *J. Geophys. Res. Solid* **122**, 9921–9930 (2017).
176. Lord, O. T. et al. The melting curve of Ni to 1 mbar. *Earth Planet. Sci. Lett.* **408**, 226–236 (2014).
177. Morard, G. et al. Fe-FeO and Fe-Fe_3C melting relations at earth's core–mantle boundary conditions: implications for a volatile-rich or oxygen-rich core. *Earth Planet. Sci. Lett.* **473**, 94–103 (2017).
178. Boccato, S. et al. Compression of liquid Ni and Co under extreme conditions explored by X-ray absorption spectroscopy. *Phys. Rev. B* **100**, 180101 (2019).
179. Morard, G. et al. Solving controversies on the iron phase diagram under high pressure. *Geophys. Res. Lett.* **45**, 11074–11082 (2018).
180. D'Angelo, P., Benfatto, M., Della Longa, S. & Pavel, N. V. Combined XANES and EXAFS analysis of Co^{2+}, Ni^{2+}, and Zn^{2+} aqueous solutions. *Phys. Rev. B* **66**, 064209 (2002). **An example of good practice.**
181. Merkling, P. J., Muñoz Páez, A., Martínez, J. M., Pappalardo, R. R. & Sánchez Marcos, E. Molecular-dynamics-based investigation of scattering path contributions to the EXAFS spectrum: the Cr^{3+} aqueous solution case. *Phys. Rev. B* **64**, 012201 (2001).
182. Persson, I., D'Angelo, P., De Panfilis, S., Sandström, M. & Eriksson, L. Hydration of lanthanoid (iii) ions in aqueous solution and crystalline hydrates studied by EXAFS spectroscopy and crystallography: the myth of the 'gadolinium break'. *Chem. Eur. J.* **14**, 3056–3066 (2008).
183. D'Angelo, P., De Panfilis, S., Filipponi, A. & Persson, I. High-energy X-ray absorption spectroscopy: a new tool for structural investigations of lanthanoids and third-row transition elements. *Chem. Eur. J.* **14**, 3045–3055 (2008).

184. Tanida, H., Sakane, H. & Watanabe, I. Solvation structures for bromide ion in various solvents by extended X-ray absorption fine structure. *J. Chem. Soc. Dalton Trans.* **15**, 2321–2326 (1994).
185. D'Angelo, P. & Pavel, N. V. Complete spectrum of multielectron excitations at the Br^- K edge X-ray absorption spectra. *Phys. Rev. B* **64**, 233112 (2001).
186. D'Angelo, P., Di Cicco, A., Filipponi, A. & Pavel, N. V. Double-electron excitation channels at the Br K edge of HBr and Br_2. *Phys. Rev. A* **47**, 2055–2063 (1993).
187. D'Angelo, P. et al. Revised ionic radii of lanthanoid(iii) ions in aqueous solution. *Inorg. Chem.* **50**, 4572–4579 (2011).
188. D'Angelo, P., Martelli, F., Spezia, R., Filipponi, A. & Denecke, M. Hydration properties and ionic radii of actinide(iii) ions in aqueous solution. *Inorg. Chem.* **52**, 10318–10324 (2013).
189. Eisenberger, P. & Kincaid, B. M. EXAFS: new horizons in structure determinations. *Science* **200**, 1441–1447 (1978).
190. Andreini, C., Bertini, I., Cavallaro, G., Holliday, G. & Thornton, J. M. Metal ions in biological catalysis: from enzyme databases to general principles. *J. Biol. Inorg. Chem.* **13**, 1205–1218 (2008).
191. Ortega, R., Carmona, A., Llorens, I. & Solari, P. L. X-ray absorption spectroscopy of biological samples. A tutorial. *J. Anal. At. Spectrom.* **27**, 2054–2065 (2012).
192. Giachini, L., Veronesi, G., Francia, F., Venturoli, G. & Boscherini, F. Synergic approach to XAFS analysis for the identification of most probable binding motifs for mononuclear zinc sites in metalloproteins. *J. Synchrotron Radiat.* **17**, 41–52 (2010).
193. D'Angelo, P. et al. Dynamic investigation of protein metal active sites: interplay of XANES and molecular dynamics simulations. *J. Am. Chem. Soc.* **132**, 14901–14909 (2010).
194. Cheung, K.-C., Strange, R. W. & Hasnain, S. S. 3D EXAFS refinement of the Cu site of azurin sheds light on the nature of structural change at the metal centre in an oxidation–reduction process: an integrated approach combining EXAFS and crystallography. *Acta Crystallogr. D* **56**, 697–704 (2000).
195. Streltsov, V. A., Ekanayake, R. S., Drew, S. C., Chantler, C. T. & Best, S. P. Structural insight into redox dynamics of copper bound N-truncated amyloid-β peptides from in situ X-ray absorption spectroscopy. *Inorg. Chem.* **57**, 11422–11435 (2018).
196. Ekanayake, R. S. K., Streltsov, V. A., Best, S. P. & Chantler, C. T. Nanostructure and dynamics of N-truncated copper amyloid-β peptides from advanced X-ray absorption fine structure. *IUCr J.* **11**, 325–346 (2024).
197. Ekanayake, R. S. K., Streltsov, V. A., Best, S. P. & Chantler, C. T. Using XAS to monitor radiation damage in real time and post-analysis and investigation of systematics of fluorescence X-ray absorption spectroscopy for Cu-bound amyloid-β. *J. Appl. Crystallogr.* **57**, 125–139 (2024).
198. Cutsail, G. E. I. et al. High-resolution extended X-ray absorption fine structure analysis provides evidence for a longer Fe ··· Fe distance in the *q* intermediate of methane monooxygenase. *J. Am. Chem. Soc.* **140**, 16807–16820 (2018).
199. Cutsail, G. E., Ross, M. O., Rosenzweig, A. C. & DeBeer, S. Towards a unified understanding of the copper sites in particulate methane monooxygenase: an X-ray absorption spectroscopic investigation. *Chem. Sci.* **12**, 6194–6209 (2021).
200. Curis, E. et al. Carboplatin and oxaliplatin decomposition in chloride medium, monitored by XAS. *J. Synchrotron Radiat.* **8**, 716–718 (2001).
201. Nicolis, I., Curis, E., Deschamps, P. & Bezaneth, S. X-ray absorption spectroscopy of low-molar-mass metallic complexes in pharmacy. *J. Synchrotron Radiat.* **10**, 96–102 (2003).
202. Messori, L. et al. X-ray absorption spectroscopy studies of the adducts formed between cytotoxic gold compounds and two major serum proteins. *J. Biol. Inorg. Chem.* **16**, 491–499 (2011).
203. Weekley, C. M. et al. Metabolism of selenite in human lung cancer cells: X-ray absorption and fluorescence studies. *J. Am. Chem. Soc.* **133**, 18272–18279 (2011).
204. Sindhupakorn, B. & Kidkhunthod, P. Structural investigation in subchondral bone of osteoarthritic knee: phosphorous *k*-edge XAS. *Radiat. Phys. Chem.* **187**, 109584 (2021).
205. Coker, V. S. et al. Probing the site occupancies of Co-, Ni-, and Mn-substituted biogenic magnetite using XAS and XMCD. *Am. Min.* **93**, 1119–1132 (2008).
206. Refait, P. et al. Mossbauer and XAS study of a green rust mineral; the partial substitution of Fe^{2+} by Mg^{2+}. *Am. Min.* **86**, 731–739 (2001).
207. Liu, W. et al. Revisiting the hydrothermal geochemistry of europium(ii/iii) in light of new in-situ XAS spectroscopy results. *Chem. Geol.* **459**, 61–74 (2017).
208. Tian, Y. et al. Speciation of nickel(ii) chloride complexes in hydrothermal fluids: in situ XAS study. *Chem. Geol.* **334**, 345–363 (2012).
209. Liu, W. et al. Speciation and thermodynamic properties for cobalt chloride complexes in hydrothermal fluids at 35–440 °C and 600 bar: an in-situ XAS study. *Geochim. Cosmochim. Acta* **75**, 1227–1248 (2011).
210. Baker, L. L., Strawn, D. G., Vaughan, K. L. & McDaniel, P. A. XAS study of Fe mineralogy in a chronosequence of soil clays formed in basaltic cinders. *Clays Clay Miner.* **58**, 772–782 (2010).
211. Giuli, G., Paris, E., Mungall, J., Romano, C. & Dingwell, D. V oxidation state and coordination number in silicate glasses by XAS. *Am. Min.* **89**, 1640–1646 (2004).
212. Morales-Pérez, A. et al. Geochemical changes of Mn in contaminated agricultural soils nearby historical mine tailings: Insights from XAS, SRD and SEP. *Chem. Geol.* **573**, 120217 (2021).
213. Castorina, E., Ingall, E. D., Morton, P. L., Tavakoli, D. A. & Lai, B. Zinc *k*-edge XANES spectroscopy of mineral and organic standards. *J. Synchrotron Radiat.* **26**, 1302–1309 (2019).
214. Ingall, E. D. et al. Phosphorus *k*-edge XANES spectroscopy of mineral standards. *J. Synchrotron Radiat.* **18**, 189–197 (2011).
215. Oakes, M. et al. Iron solubility related to particle sulfur content in source emission and ambient fine particles. *Environ. Sci. Technol.* **46**, 6637–6644 (2012).
216. Siebecker, M. G., Chaney, R. L. & Sparks, D. L. Natural speciation of nickel at the micrometer scale in serpentine (ultramafic) topsoils using microfocused X-ray fluorescence, diffraction, and absorption. *Geochem. Trans.* **19**, 1–16 (2018).
217. McDaniel, M. F. M. et al. Relationship between atmospheric aerosol mineral surface area and iron solubility. *ACS Earth Space Chem.* **3**, 2443–2451 (2019).
218. Negassa, W. et al. Phosphorus speciation in agro-industrial byproducts: sequential fractionation, solution ^{31}P NMR, and P *K*- and $L_{2,3}$-edge XANES spectroscopy. *Environ. Sci. Technol.* **44**, 2092–2097 (2010).
219. Struis, R. P., Ludwig, C., Lutz, H. & Scheidegger, A. M. Speciation of zinc in municipal solid waste incineration fly ash after heat treatment: an X-ray absorption spectroscopy study. *Environ. Sci. Technol.* **38**, 3760–3767 (2004).
220. Oakes, M., Weber, R., Lai, B., Russell, A. & Ingall, E. Characterization of iron speciation in urban and rural single particles using XANES spectroscopy and micro X-ray fluorescence measurements: investigating the relationship between speciation and fractional iron solubility. *Atmos. Chem. Phys.* **12**, 745–756 (2012).
221. Brandes, J. A., Ingall, E. & Paterson, D. Characterization of minerals and organic phosphorus species in marine sediments using soft X-ray fluorescence spectromicroscopy. *Mar. Chem.* **103**, 250–265 (2007).
222. McCanta, M. C. et al. In situ measurement of ferric iron in lunar glass beads using Fe-XAS. *Icarus* **285**, 95–102 (2017).
223. Sier, D. et al. High accuracy mass attenuation measurement and atomic structure determination of zinc selenide through the X-ray extended range technique. *J. Synchrotron Radiat.* **27**, 1262–1277 (2020).
224. Chantler, C. T. & Bourke, J. D. Low-energy electron properties: electron inelastic mean free path, energy loss function and the dielectric function. Recent measurements, applications, and the plasmon-coupling theory. *Ultramicroscopy* **201**, 38–48 (2019).
225. Tran, N. T. T. et al. A new satellite of manganese revealed by extended-range high-energy-resolution fluorescence detection. *J. Synchrotron Radiat.* **30**, 605–612 (2023).
226. Frahm, R. Quick scanning EXAFS: first experiments. *Nucl. Instrum. Methods Phys. Res. Sect. A Accel. Spectrom. Detect. Assoc. Equipment* **270**, 578–581 (1988).
227. Fonda, E. et al. The SAMBA quick-EXAFS monochromator: XAS with edge jumping. *J. Synchrotron Radiat.* **19**, 417–424 (2012).
228. Nordfors, B. The statistical error in X-ray absorption measurements. *Arkiv Fysik* **18**, 37–47 (1960).
229. Creagh, D. C. & Hubbell, J. H. Problems associated with the measurement of X-ray attenuation coefficients. I. Silicon. Report of the International Union of Crystallography X-ray Attenuation Project. *Acta Crystallogr. A* **43**, 102–112 (1987).
One of the first detailed reports of reproducibility, portability and transferability for X-ray absorption spectroscopy.
230. Stern, E. A. Number of relevant independent points in X-ray-absorption fine-structure spectra. *Phys. Rev. B* **48**, 9825–9827 (1993).
231. Newville, M., Boyanov, B. I. & Sayers, D. E. Estimation of measurement uncertainties in XAFS data. *J. Synchrotron Radiat.* **6**, 264–265 (1999).
232. Sayers, D. E. Report of the International XAFS Society Standards and Criteria Committee. *IXS Standards and Criteria Subcommittee* http://ixs.iit.edu/subcommittee_reports/sc/ (2000).
233. Chantler, C. T., Barnea, Z., Tran, C. Q., Tiller, J. B. & Paterson, D. Precision X-ray optics for fundamental interactions in atomic physics, resolving discrepancies in the X-ray regime. *Opt. Quantum Electron.* **31**, 495–505 (1999).
234. Chantler, C. T., Tran, C. Q., Paterson, D., Barnea, Z. & Cookson, D. J. Monitoring fluctuations at a synchrotron beamline using matched ion chambers: 1. modelling, data collection, and deduction of simple measures of association. *X-Ray Spectrom.* **29**, 449–458 (2000).
235. Chantler, C. T., Tran, C. Q., Paterson, D., Cookson, D. & Barnea, Z. X-ray extended-range technique for precision measurement of the X-ray mass attenuation coefficient and Im(*f*) for copper using synchrotron radiation. *Phys. Lett. A* **286**, 338–346 (2001).
236. Chantler, C. T. et al. High-accuracy X-ray absorption spectra from mM solutions of nickel (II) complexes with multiple solutions using transmission XAS. *J. Synchrotron Radiat.* **22**, 1008–1021 (2015).
237. Chantler, C. T. in *International Tables for Crystallography* Vol. I. Ch. 7.4 (eds Chantler, C. T., Bunker, B. A. & Boscherini, F.) 867–925 (Kluwer Academic Publishers, 2024).
238. Diaz-Moreno, S. XAFS data collection: an integrated approach to delivering good data. *J. Synchrotron Radiat.* **19**, 863–868 (2012).
239. Abe, H. et al. Improving the quality of XAFS data. *J. Synchrotron Radiat.* **25**, 972–980 (2018).
240. Chantler, C. T. et al. A call for a round robin study of XAFS stability and platform dependence at synchrotron beamlines on well defined samples. *J. Synchrotron Radiat.* **25**, 935–943 (2018).
241. Mika, J. F., Martin, L. J. & Barnea, Z. X-ray attenuation of silicon in the energy range 25–50 keV. *J. Phys. C* **18**, 5215–5223 (1985).
242. Creagh, D. C. & Hubbell, J. H. Problems associated with the measurement of X-ray attenuation coefficients. III. Carbon. Report on the International Union of Crystallography X-ray Attenuation Project. *Acta Crystallogr. A* **46**, 402–408 (1990).
243. Kelly, S. D. et al. Comparison of EXAFS foil spectra from around the world. *J. Phys. Conf. Ser.* **190**, 012032 (2009).
244. Newton, M. A. Operando catalysis using synchrotron methods. *Catal. Struct. React.* **3**, 2–4 (2017).

245. Catlow, C. R. A. Operando structural science of functional materials. *IUCrJ* **8**, 703–704 (2021).
246. Favaro, M., Artiglia, L. & Mun, B. S. In situ/operando investigation of catalytic and electrocatalytic interfaces. *J. Phys. D Appl. Phys.* **55**, 060201 (2021).
247. Newton, M. A. & van Beek, W. Combining synchrotron-based X-ray techniques with vibrational spectroscopies for the in situ study of heterogeneous catalysts: a view from a bridge. *Chem. Soc. Rev.* **39**, 4845–4863 (2010).
248. Bentrup, U. Combining in situ characterization methods in one set-up: looking with more eyes into the intricate chemistry of the synthesis and working of heterogeneous catalysts. *Chem. Soc. Rev.* **39**, 4718–4730 (2010).
249. Povia, M. et al. Combining SAXS and XAS to study the operando degradation of carbon-supported Pt-nanoparticle fuel cell catalysts. *ACS Catal.* **8**, 7000–7015 (2018).
250. Gaur, A. et al. Structural dynamics of an iron molybdate catalyst under redox cycling conditions studied with in situ multi edge XAS and XRD. *Phys. Chem. Chem. Phys.* **22**, 11713–11723 (2020).
251. Sun, H. et al. XAS/DRIFTS/MS spectroscopy for time-resolved operando study of integrated carbon capture and utilisation process. *Sep. Purif. Technol.* **298**, 121622 (2022).
252. Glatzel, P. et al. Reflections on hard X-ray photon-in/photon-out spectroscopy for electronic structure studies. *J. Electron Spectrosc. Relat. Phenom.* **188**, 17–25 (2013).
253. Hayama, S. et al. Photon-in/photon-out spectroscopy at the I20-scanning beamline at diamond light source. *J. Condens. Matter Phys.* **33**, 284003 (2021).
254. Kas, J. J., Rehr, J. J., Glover, J. L. & Chantler, C. T. Comparison of theoretical and experimental Cu and Mo *K*-edge XAS. *Nucl. Instrum. Methods A* **619**, 28–32 (2010).
255. Joly, Y. et al. Self-consistency, spin–orbit and other advances in the FDMNES code to simulate XANES and RXD experiments. *J. Phys. Conf. Ser.* **190**, 012007 (2009).
256. Gilmore, K. et al. Efficient implementation of core-excitation Bethe–Salpeter equation calculations. *Comput. Phys. Commun.* **197**, 109–117 (2015).
257. Dean, J. W., Pushkarna, P., Melia, H. A., Nguyen, T. V. B. & Chantler, C. T. Theoretical calculation of characteristic radiation: multiconfiguration Dirac–Hartree–Fock calculations in scandium K *α* and K *β*. *J. Phys. B* **55**, 075002-1–13 (2022).
258. Timoshenko, J., Lu, D., Lin, Y. & Frenkel, A. I. Supervised machine-learning-based determination of three-dimensional structure of metallic nanoparticles. *J. Phys. Chem. Lett.* **8**, 5091–5098 (2017).
259. Rankine, C. D., Madkhali, M. M. M. & Penfold, T. J. A deep neural network for the rapid prediction of X-ray absorption spectra. *J. Phys. Chem. A* **124**, 4263–4270 (2020).
260. Zimmermann, P. et al. Modern X-ray spectroscopy: XAS and XES in the laboratory. *Coord. Chem. Rev.* **423**, 213466 (2020).
261. Chantler, C. T., Bunker, B. A. & Boscherini, F. in *International Tables for Crystallography* Vol. I, Ch. 1.4 (eds Chantler, C. T., Bunker, B. A. & Boscherini, F.) 16–20 (Kluwer Academic Publishers, 2024).
262. Ghigna, P. et al. Lithiation mechanism in high-entropy oxides as anode materials for li-ion batteries: an operando XAS study. *ACS Appl. Mater. Interfaces* **12**, 50344–50354 (2020).
263. Augustyn, V. et al. High-rate electrochemical energy storage through Li^+ intercalation pseudocapacitance. *Nat. Mater.* **12**, 518–522 (2013).
264. Xie, Y. et al. Role of surface structure on Li-ion energy storage capacity of two-dimensional transition-metal carbides. *J. Am. Chem. Soc.* **136**, 6385–6394 (2014).
265. Zhuo, Z. et al. Breathing and oscillating growth of solid–electrolyte-interphase upon electrochemical cycling. *Chem. Commun.* **54**, 814–817 (2018).
266. Dietrich, C. et al. Spectroscopic characterization of lithium thiophosphates by XPS and XAS — a model to help monitor interfacial reactions in all-solid-state batteries. *Phys. Chem. Chem. Phys.* **20**, 20088–20095 (2018).
267. Cui, Y. et al. (De)lithiation mechanism of Li/SeS_x (x=0–7) batteries determined by in situ synchrotron X-ray diffraction and X-ray absorption spectroscopy. *J. Am. Chem. Soc.* **135**, 8047–8056 (2013).
268. Torchio, R., Mathon, O. & Pascarelli, S. XAS and XMCD spectroscopies to study matter at high pressure: probing the correlation between structure and magnetism in the 3*d* metals. *Coord. Chem. Rev.* **277**, 80–94 (2014).
269. Roe, A. et al. X-ray absorption spectroscopy of iron-tyrosinate proteins. *J. Am. Chem. Soc.* **106**, 1676–1681 (1984).
270. Mölders, N., Schilling, P. J., Wong, J., Roos, J. W. & Smith, I. L. X-ray fluorescence mapping and micro-XANES spectroscopic characterization of exhaust particulates emitted from auto engines burning MMT-added gasoline. *Environ. Sci. Technol.* **35**, 3122–3129 (2001).
271. Werner, F. & Prietzel, J. Standard protocol and quality assessment of soil phosphorus speciation by P *k*-edge XANES spectroscopy. *Environ. Sci. Technol.* **49**, 10521–10528 (2015).
272. Moseley, H. G. J. The high frequency spectra of the elements. *Phil. Mag.* **26**, 1024–1034 (1913).
273. de Broglie, M. Sur une nouveau procédé permettant d'obtenir la photographie des spectres de raies des rayons Röntgen. *Comptes Rendus* **157**, 924–926 (1913).
274. Fricke, H. The *K*-characteristic absorption frequencies for the chemical elements magnesium to chromium. *Phys. Rev.* **16**, 202–215 (1920).
275. Sayers, D. E., Stern, E. A. & Lytle, F. W. New technique for investigating noncrystalline structures: Fourier analysis of the extended X-ray-absorption fine structure. *Phys. Rev. Lett.* **27**, 1204–1207 (1971).
276. Sayers, D. E., Lytle, F. W. & Stern, E. A. Structure determination of amorphous Ge, GeO_2 and GeSe by Fourier analysis of extended X-ray absorption fine structure (EXAFS). *J. Non-Cryst. Solids* **8**–**10**, 401–407 (1972).
277. Barton, J. J. & Shirley, D. A. Curved-wave-front corrections for photoelectron scattering. *Phys. Rev. B* **32**, 1892–1905 (1985).
278. Gurman, S. J., Binsted, N. & Ross, I. A rapid, exact curved-wave theory for EXAFS calculations. *J. Phys. C* **17**, 143–151 (1984).
279. Lee, P. A. & Beni, G. New method for the calculation of atomic phase shifts: application to extended X-ray absorption fine structure (EXAFS) in molecules and crystals. *Phys. Rev. B* **15**, 2862–2883 (1977).
280. Deslattes, R. D. & Henins, A. X-ray to visible wavelength ratios. *Phys. Rev. Lett.* **31**, 972 (1973).
281. Cohen, E. & Taylor, B. The 1986 adjustment of the fundamental physical constants. *Rev. Modern Phys.* **59**, 1121 (1987).
282. Westre, T. E. et al. GNXAS, a multiple-scattering approach to EXAFS analysis: methodology and applications to iron complexes. *J. Am. Chem. Soc.* **117**, 1566–1583 (1995).
283. Rehr, J. J. & Albers, R. C. Theoretical approaches to X-ray absorption fine structure. *Rev. Mod. Phys.* **72**, 621–654 (2000).
Popular review of approaches to X-ray absorption fine structure theory, for 2000.
284. Bourke, J. D., Chantler, C. T. & Witte, C. Finite difference method calculations of X-ray absorption fine structure for copper. *Phys. Lett. A* **360**, 702–706 (2007).
285. Chantler, C. T. & Bourke, J. D. X-ray spectroscopic measurement of photoelectron inelastic mean free paths in molybdenum. *J. Phys. Chem. Lett.* **1**, 2422–2427 (2010).
286. Guda, A. A. et al. Quantitative structural determination of active sites from in situ and operando XANES spectra: from standard ab initio simulations to chemometric and machine learning approaches. *Catal. Today* **336**, 3–21 (2019).

Author contributions

Introduction (C.T.C., G.B., P.D. and S.D.-M.); Experimentation (C.T.C., G.B., P.D. and S.D.-M.); Results (C.T.C., G.B., P.D. and S.D.-M.); Applications (C.T.C., G.B., P.D. and S.D.-M.); Reproducibility and data deposition (C.T.C., G.B., P.D. and S.D.-M.); Limitations and optimizations (C.T.C., G.B., P.D. and S.D.-M.); Outlook (C.T.C., G.B., P.D. and S.D.-M.); overview of the Primer (all authors).

Competing interests

The authors declare no competing interests.

Additional information

Supplementary information The online version contains supplementary material available at https://doi.org/10.1038/s43586-024-00366-8.

Peer review information *Nature Reviews Methods Primers* thanks the anonymous reviewers for their contribution to the peer review of this work.

Related links

lightsources.org: https://lightsources.org/
Mucal periodic table: http://www.csrri.iit.edu/periodic-table.html
X-ray data booklet: http://xdb.lbl.gov